Revision 1

Targeting Mixtures of Jarosite and Clay Minerals for Mars Exploration

Nancy W. Hinman*[a], Janice L. Bishop[b,c], Virginia C. Gulick [b,c], J. Michelle Kotler Dettmann[a,1], Paige Morkner[d,2], Genesis Berlanga[c,d,3], Ruth M. Henneberger[e,4], Peter Bergquist[f], Charles Doc Richardson[a,5], Malcolm R. Walter[g], Lindsay A. MacKenzie[a,6], Roberto P. Anitori[e,7], Jill R. Scott[i]

[a] Department of Geosciences, 32 Campus Dr., MC 1296, University of Montana, Missoula, MT USA 59812-1296; nancy.hinman@umontana.edu

[b] The SETI Institute, Mountain View, CA USA 94043

[c] NASA Ames Research Center, Moffett Field, CA USA 94035

[d] NASA Internship Program, NASA Ames Research Center, Moffett Field, CA 94035

[e] Department of Chemistry and Biomolecular Science, Macquarie University, North Ryde 2109, NSW, Australia;

[f] Department of Molecular Medicine and Pathology, University of Auckland School of Medicine, Auckland, New Zealand

[g] Australian Centre for Astrobiology, University of New South Wales, Sydney, 2052, Australia.

[h] Department of Biology, University of Portland, OR USA 97203-5798

[i] Chemical Sciences, Idaho National Laboratory, Idaho Falls, ID 83415

[1] Present address: European Space Agency ECSAT, Fermi Avenue, Harwell Campus, Didcot, United Kingdom.

[2] Present address: ORISE Fellow, National Energy Technology Laboratory, Albany, OR, USA

[3] Blue Marble Space Institute of Science at NASA Ames

[4] Present address: Institute of Molecular Health Sciences, Swiss Federal Institute of Technology (ETH), 8093 Zürich, Switzerland

[5] Present address: NewFields, Helena, MT USA

[6] Present address: Eastern Washington State University, Cheney, WA USA

[7] Present address: Biology Department, Clark College, Vancouver, WA USA

*Corresponding author

Keywords: Mars, surface; Astrobiology; Exobiology; Spectroscopy

Running Title: Jarosite Mixtures for Mars Exploration

Abstract

Terrestrial thermal environments can serve as analogs for subsurface environments in the search for life because they regularly host microbial communities, which may leave behind biosignatures. This study focused on an acid-sulfate hydrothermal site as an analog for a potentially habitable environment on Mars. A weathered boulder in the thermal area was dissected, revealing an interior marked with disconnected horizons of differently colored materials, very low pH, and increasing temperature. The mineralogy comprised weathering products from andesite (kaolinite, quartz, clinoptilolite) along with sulfate salts (alunite, jarosite, tschermigite, and copiapite) formed by oxidation of sulfide and ferrous iron. Characterization of organic matter in this boulder and several soil samples yielded interesting but surprising results. Both mass spectrometry and Raman spectroscopy identified organic compounds in portions of the soils and the boulder. Jarosite-associated samples showed more numerous and diverse organic signatures than did Al-bearing silicate samples, despite the lower total organic carbon content of the jarosite-associated soils (0.69 ± 0.07 wt% C_{org}) compared to the Al-bearing samples (1.28 ± 0.13 wt% C_{org}). Results from our geochemical, mineralogical, and spectroscopic study of hydrothermal alteration products and salts inform the heterogeneous distribution of inorganic and organic materials that could delineate habitats and demonstrate the limits on organic matter detectability using different analytical techniques. Further, we relate our measurements and results relate directly to current and upcoming martian missions, and we provide recommendations for detection and characterization of minerals and organics as biosignatures on Mars using instruments on future missions.

1 Introduction

Multiple geologic environments with evidence of aqueous alteration processes have been identified on Mars (e.g., Bibring et al., 2006; Murchie et al., 2009; Ehlmann and Edwards, 2014). Carter et al. (2013) documented numerous sites on the surface of Mars containing hydrous minerals, including phyllosilicates and sulfate minerals, over the surface of Mars using data from the Observatoire pour la Minéralogie, l'Eau, les Glaces et l'Activité) (OMEGA) and Compact Reconnaissance Imaging Spectrometer for Mars (CRISM) data. Most sites are located in ancient outcrops in Noachian and Hesperian terrains. The recent selection of Jezero crater, which has been interpreted as an episodic paleolake, delta, and/or fluvial plain; Ehlmann et al., 2008; Goudge et al., 2015a,b) as the target for the Mars 2020 landing site emphasizes the relevance of understanding the potential for biosignature preservation in rocks containing carbonates, sulfates, and clay minerasl in the search for evidence of life. Jezero crater contains a volcanic unit dated at ~3.45 Ga that embays the sedimentary fan unit to be investigated by Mars 2020 (Goudge et al., 2015a). Volcanic heat in this region likely produced hydrothermal activity, which could have led to the formation of acid-sulfate thermal environments given the acidic nature of volcanic gases. The Mars 2020 rover may be able to identify acid-sulfate minerals, such as jarosite ($K(Fe_3(SO_4)_2(OH)_6)$) and other sulfates, that are not observed from orbit. Terrestrial acid-sulfate environments may closely resemble those on early Mars (Nna-Mvondo and Martinez-Frias, 2007). Unfortunately, the conditions that could best preserve evidence of ancient life on Mars remain confounding and unclear to the scientific community, and thus additional studies in this area are needed (Walter and Des Marais, 1993, 1999; Farmer and Des Marais, 1999; Des Marais, 2001, 2008; Summons et al., 2011).

Retention and detection are both important to the prospect of finding organic matter and/or biosignatures during any surface mission. Minerals that retain organic matter or that promote its detection are of value, not only to the identification of organic matter, but to the prospects of finding potential biosignatures in any surface mission. Indeed, acid-sulfate terrestrial hot springs remain high priority analog sites to better interpret the results of future Mars missions (Fairen et al 2010; Martins et al., 2017).

On Earth, jarosite forms in sulfate-rich environments where Fe(II) is oxidized. For example, jarosite and related sulfates form in acidic waters associated with sulfide oxidation (e.g., Burns 1987; Alpers et al., 1989; Bigham and Nordstrom, 2000; Jones and Renaut, 2007), in acid sulfate soils near volcanic vents (e.g., Zimbelman et al., 2005; Schiffman et al., 2006; Bishop et al., 2007), and where SO_2 has oxidized, i.e. at the interface of Fe(II)-bearing rocks and sulfate-rich waters, such as basalt surfaces in contact with oxidizing fluids (e.g., Golden et al., 2005; Chemtob et al., 2010; Schaef et al., 2014). Synthetic jarosite phases are produced in laboratory experiments abiotically at very high temperatures (e.g., Kotler et al. 2008) and biotically at lower temperatures. Khoshkhoo et al. (2015) found that jarosite formed in experiments designed to compare abiotic leaching and bioleaching of copper from sulfide ores. Additionally, jarosite formed in bioleaching experiments in which hyperthermophilic iron oxidizing archaea (*Acidianus*, *Metallosphaera*, and *Sulfolobus*) oxidized Fe(II) in the presence of sulfuric acid at elevated temperature (70°C) (Kaksonen et al. (2016)). We can conclude that biological processes obviate the need for the high temperature (275°C) required for abiotic Fe(II) oxidation (e.g., Kotler et al., 2008) and consequently, jarosite may reflect potential biosignatures among an array of organic compounds.

Minerals in the jarosite group have been identified on Mars (e.g.,Klingelhöfer et al., 2004; Farrand et al., 2009; Ehlmann and Mustard, 2012) in association with Mg- and Ca-sulfates, phosphates, and opaline silica (Nachon et al., 2017) and with sedimentary rocks at Gale Crater by the Mars Science Laboratory rover (Bristow et al., 2018). And other landing sites considered for Mars 2020 contain iron or aluminium sulfate minerals. For example, the NE Syrtis site features jarosite-bearing outcrops (Ehlmann and Mustard, 2012) and the Mawrth Vallis site contains both jarosite and alunite (Bishop et al. 2018; Farrand et al., 2009; Sessa et al., 2018). Terrestrial jarosite-bearing field sites provide insight into the potential for biosignature detection and retention and will contribute toward our understanding of such sites on Mars.

Fortunately, jarosite minerals can be identified spectroscopically through a variety of methods (e.g., Bishop and Murad, 2005; Ling et al., 2016; Singh et al., 2016) and more in-depth investigations have revealed that jarosite can act as a host mineral for the storage of organic compounds (Kotler et al., 2008). To determine the potential for detection and identification of organic matter in hot acid-sulfate environments, we address the following questions in this study: (1) what geochemical and mineralogical conditions prevail in such environments? and (2) do some mineralogical combinations have a higher potential than others for aiding detection of organic compounds? We looked for evidence of the presence of organic matter in extreme volcanic environments to better characterize potential acid-sulfate astrobiological targets on Mars. To achieve this goal, we examined the benefits and constraints of combining a suite of techniques. Here we present the results of a geochemical, mineralogical, and spectroscopic study of mineral soil and a hydrothermally altered boulder at Washburn Hot Springs, Yellowstone National Park, Wyoming, USA. We explored the ability of different techniques to detect mineral phases and organic matter (S1). Such information will be useful for application to the Mars 2020

missions' Scanning Habitable Environments with Raman and Luminescence for Organics and Chemicals (SHERLOC) measurements; Beegle et al., 2015) and to ExoMars Mars Organic Mass Analyzer Laser Desorption Instrument (MOMA-LDI) measurements (Goetz et al., 2016).

1.1 Site Description

Washburn Hot Springs (WHS; ~ 94,000 m^2) is a mainly dry thermal area located on the northeast flank of an Eocene andesitic volcano on the rim of the Yellowstone Caldera within Yellowstone National Park (Fig. 1, UTM: 545280, 4957188). The WHS thermal area is close to the contact between Eocene andesitic lavas and Plio-Pleistocene colluvium from more recent eruptions (2.2 to 0.68 ma) of the rhyolitic Yellowstone volcano (Christiansen, 2001). Mainly, though, andesitic boulders and colluvium surround the thermal area. The thermal area itself comprises alteration products of the surrounding materials, while steam and acidic gases have leached minerals from the original rock and related soils. Steam condenses in small, vigorously degassing hot springs. The pH of the hot springs there ranges from ~ 3 to 5 (Fishbain et al., 2003; Rodman, 1996), which is higher than the typical pH 1.5 to 2.5 of other acid-sulfate spring areas in Yellowstone (Fournier, 1989) (see S2).

The study site comprised the acid-sulfate area of Washburn Hot Springs, which is located on a steep slope with a few hot springs and above several other large hot springs at the base of the slope. The acid-sulfate area had "extensive diffuse gas seeps and an unknown number of fumaroles." (http://www.rcn.montana.edu/, accessed 6/26/19). Few studies have been conducted at WHS. Fournier (1989) analyzed two hot springs at the base of the WHS thermal area, both of which had higher pH (6.2) than the water analyzed herein (3.64 - 4.55) and concluded that ammonia is likely responsible for the higher pH and "probably derived from distillation of buried

sediments". Spear et al. (2005) found similar pH values at the base of the WHS thermal area. Both studies confirmed that WHS emits H_2S gas, which oxidizes to SO_4^{2-}, which can then combine with available Fe and K^+ to form jarosite. We sampled in the topographically higher acid-sulfate area of WHS and consequently the physicochemical conditions in our study area differed from the hot springs at the base of the WHS area. Additional site description is provided in S2.

2 Approach and Methodology

Four soil sites (W1, W4, WS5, WS8), a disintegrating boulder (W2), and a background site (W3) were sampled (Fig. 1) for geochemistry (W1, W2, W3, W4), mineralogy (W1, W2, WS5, WS8), and spectroscopy (W1, W2, WS5, WS8) studies (Table 1). The sites were selected to represent the common surface materials (W1, see Fig. 2) and the uncommon surface features (W2, WS5, and WS8, see Fig. 2). All sampling sites were dry. W1 was approximately 3 meters from any thermal feature. W2 was over 50 meters from a small runoff channel. W4 was approximately 50 m and uphill from Ink Pot spring (WWS5, ~ 5 m^2, formally named WHSNN013, Yellowstone RCN database, http://www.rcn.montana.edu/, accessed 5/20/19). WS5 and WS8 were within 2 m of Ink Pot spring and a runoff channel, respectively.

2.1 Sample Collection

2.1.1 Field Analyses, Sample Collection, and Subsample Selection. Temperature and pH of the soils and soil slurries were measured in the field with an Orion pH meter (Thermo Fisher Scientific, Waltham, MA, USA) equipped with a Sensorex 200C combination electrode (Sensorex, Garden Grove, CA, USA) and Orion steel temperature sensor (Thermo Fisher

Scientific, Waltham, MA, USA). Soil pH was measured in the field by preparing slurries in deionized H_2O and applying the same procedures used to measure the pH and temperature of water samples. The temperature of soil samples was measured in the field with a Fluke 51 II temperature meter (Fluke Corporation, Everett, WA, USA).

Samples for bulk geochemical analyses (~ 100 g) were collected with acid-washed, plastic utensils and placed in plastic centrifuge tubes. Subsamples (<1g) of W2 were isolated in the field (plastic centrifuge tubes) and in the laboratory (glass scintillation vials) based on differences in color and texture. W2 was subsampled in the field (plastic centrifuge tubes) for spatial correlation of visual features (color and texture) with temperature and pH (Fig. 2). W2 was further subsampled in the laboratory to better isolate materials of different color and texture. Small samples (<1g) were collected at WS5 and WS8. Plastic was used to ensure the integrity of trace element compositions but does introduce the potential for contamination of organic matter by plasticizers, typically phthalates. Organic contamination is discussed in SI.3. Solid samples were air dried and stored at ambient temperatures.

2.2 Analytical Methods

2.2.1 Geochemical and Physical Characterization. Geochemical characteristics (major elements, minor elements, and organic carbon) were measured on bulk samples of 100 g of homogenized material (W1, W2, W3, W4). Major element concentrations were measured by X-ray fluorescence spectrometry (XRF) on lithium-metaborate-fused glass discs. Minor elements were analyzed by inductively coupled plasma emission mass spectrometry (ICPMS) on samples digested with a multi-acid technique. The C and S analyses were performed by a combustion / infrared method ((Leco SC632-Series, ASTM method E-1915-97). Carbonate minerals are not

stable at the pH (3.64-4.55), pressure, and temperature of this environment; inorganic carbon is only present as CO_2 gas at this temperature and atmospheric pressure (Stumm and Morgan, 2012). Consequently, any carbon detected in our samples would be organic carbon. A commercial laboratory (SGS Canada, Lakefield, Ontario, Canada) performed the XRF, ICPMS, and C and S analyses. Their reported reproducibility and error as within ±10 wt% of the analytical value.

Scanning electron microscopy imagery and chemistry (SEM/EDS) were collected from un-homogenized carbon-coated samples mounted on aluminum stubs, with a Hitachi S-4700 cold field emission SEM (Hitachi, Tokyo, Japan) and a Quartz One energy dispersive spectrometer operated with Quartz Imaging Xone software (Quartz Imaging, Vancouver, B.C., Canada) at the University of Montana (UM).

Laser desorption and ionization (LDI) Fourier transform ion cyclotron resonance (FT-ICR) mass spectrometry (MS) (LDI-FT-ICR MS, herein LD-FTMS) was used to survey inorganic and organic compositions and to complement other techniques. LDI brings an advantage to deploying this sample introduction method on Mars in future flight missions or as a screening tool for sample return missions. The laser desorbs ions and neutral species from the sample directly. No sample preparation is required, unlike matrix-assisted laser desorption ionization (MALDI) that uses an introduced matrix to desorb and ionize analytes. Because the native minerals serve as the matrix, the term GALDI (geomatrix-assisted laser desorption and ionization) (Yan et al., 2007a) was coined.. Other techniques may require that the sample be powdered, heated, or dissolved prior to analysis. FTMS has a lower detection limit than other mass spectrometric techniques (Kotler et al., 2008; Richardson et al., 2008; Heeren et al., 2004) and can provide correlation between inorganic and organic compositions in a single laser shot

(spot size 6 μm). The LD-FTMS used here had "high mass accuracy (error ± 0.003 amu), high resolution (typically >10,000), high sensitivity (~200 ions for peaks with S/N ~3, and high spatial resolution (spot size ~6 μm)" (Yan et al., 2006). In addition, the LD-FTMS in this study has highly accurate laser scanning (Scott and Tremblay, 2002) that provides mapping capabilities (Scott et al., 2006, Yan et al., 2006, 2007a, b) to provide spatial correlations.

The LD-FTMS was equipped with a 7T Oxford magnet (Oxford, England), a 355 nm Nd:YAG laser (Continuum, Santa Clara (CA)), an Odyssey control and data acquisition system (Finnigan FT/MS, Bremen, Germany), and laboratory-designed automated software for data acquisition and interpretation (McJunkin et al. 2002, 2010; Yan et al., 2006). Sample handling procedures and FTMS parameters are described in detail elsewhere (Yan et al., 2007a,b; Kotler et al., 2008). Briefly, a Nd-YAG laser (Continuum, Santa Clara, CA) using 355 nm wavelength, 6 ns pulse, and fluence of 1 x 10^8 W/cm^2 was used to collect spectra (Yan et al., 2007b). Experiments at different laser energies were not performed on these samples. We know that desorption is matrix-dependent for mono-mineralic materials (Yan et al., 2007b) but the laser energy for this experiment was not optimized for these mixed-matrix samples. Instead, we used the same fluence optimized for the minerals reported in Yan et al. (20007b). The sample was 0.5 cm from the front trap plate of the FTMS cell. Baseline-corrected, zero-filled raw data were analyzed by Fourier transform to produce the mass spectra. A chemical image of the sample was generated using an automatic mapping function with very high reproducibility for location return. Composition assignments were made according to procedures described previously (Kotler et al., 2008; Richardson et al. 2008). Briefly, two parameters aid in identifying the ion attributed to a particular peak. The first is mass-to-charge ratio (m/z), which locates the peak within the spectrum, and mass defect, which is the difference between the integer or nominal

mass and the actual measured mass (e.g., Kotler et al., 2008). The mass defect is extremely valuable in distinguishing organic from inorganic species and in assigning compositions. Kotler et al. (2008) provide a detailed explanation for the assignment of compositions (stoichiometries). Our focus was on species with m/z less than 1000 amu and consequently, compositions are constrained to be within 0.003 amu of the exact mass of the most abundant isotope, e.g., mass of ^{1}H is 1.007825 based on ^{12}C mass of 12.000000. In this range (±0.003 amu), we can distinguish among between compositions to ±3 in the third decimal place. Table 4 in Kotler et al. (2008) illustrates the application of error to the compositional assignments. In their table, the nominal mass is listed as column headers. The exact masses for the corresponding nominal mass are listed in the columns for each theoretical structure. If the observed isotope mass is compared with the calculated masses for each theoretical composition in the rows below and the absolute difference between the observed mass is greater than 0.003 then that composition is eliminated. In their table, only one theoretical composition matches the observed mass within the margin of error. We used this same procedure to assign compositions.

For this study, hundreds of spectra were collected on these samples and representative spectra were chosen to report here. Analyses by geomatrix-assisted laser desorption and ionization Fourier transform ion cyclotron resonance mass spectrometry (GALDI-FT-ICR MS or herein, GALDI-FTMS) was performed at the Idaho National Laboratory (INL), Idaho Falls, ID. FT-ICR theory is covered in detail by Marshall and Verdun (1990) and summarized by Comisarow (1993). Dienes et al. (1996) and Heeren et al. (2004) provide thorough reviews of FT-ICR applications and analysis techniques. Further description of the method is provided in S3.

2.2.2 Spectroscopic Characterization. Specimens were subsampled for visible/near infrared (VNIR) reflectance and Raman spectroscopy based on observable color (buff, yellow, gray). Subsamples are labeled with the primary sample name followed by a letter and one-word description of the material (e.g., crumbles, particulate, yellow). VNIR reflectance spectra were acquired using an Analytical Spectral Devices (ASD Inc; now part of Malvern Panalytical) FieldSpecPro FR spectroradiometer covering the 0.35-2.5 µm region under ambient conditions. The spectral resolution is 3 nm from 0.35-1.0 µm and 10 nm from 1.0-2.5 µm. Spectra were acquired with a contact probe on a sample in a black Teflon dish, and spectra were calibrated against a white Spectralon panel. The spot size for VNIR is about 12 mm. Each sample was measured at least twice for 100 scans and the data were averaged. Several Raman spectra were taken in transects across each sample using a dual excitation probe (with 532 nm and 785 nm lasers) from EIC Laboratories, Inc. The spectral range and resolution is 130-4000 cm^{-1} at 13 cm^{-1} (FWHM) (532 nm) and 190-2900 cm^{-1} at 8 cm^{-1} (FWHM) (785 nm), respectively. The spot size for Raman spectroscopy is 50 µm. The sample powders were mounted on clean Pyrex glass slides in sufficiently thick layers to obtain several good spectra in a grid or transect. Raman spectra of native subsample chunks were measured as well. Raman spectra were collected at NASA Ames Research Center (NASA ARC), and visible/near infrared (VNIR) reflectance spectra were collected at the SETI Institute (SETI). Both analyses were conducted on small un-homogenized subsamples to determine and compare detection and distribution of minerals and organic matter.

2.2.3 X-ray Diffraction Characterization. The mineralogy was analyzed with a PANalytical X'Pert Pro (Malvern PANalytical, Almelo, Netherlands) with Cu radiation (1.5406 Å) on powders homogenized with an agate mortar and pestle and then mounted on frosted glass

slides. XRD patterns were matched to International Centre for Diffraction Data (ICDD, PDF-2) standards using PANalytical High Score Plus software (Malvern PANalytical, Almelo, Netherlands) at the UM Earth Materials Identification Facility. Phases were identified using a combination of automated and manual matching. Quantification of mineral phases present was performed by Rietveld refinement (Bish and Post, 1993; Chipera and Bish, 2013) with PANalytical High Score Plus software.

3 Results

The temperature and pH of acid-sulfate soils varied among the sites and with respect to the background site; this background site had a temperature between 24.4 and 29°C and a pH of 3.4 – 3.6, indicating exposure to some thermal influence at this location. The properties of the disintegrating boulder (W2) varied as a function of depth within the boulder (Table 1, Fig. 2). In water, temperatures were high (77.5°C and 43.7° C, respectively) and pH values were low (3.65 and 4.55, respectively) in the runoff channel (WWS8) and Ink Pot Hot Spring (WWS5) (S4). All field parameters are listed in Table 1 and discussed below.

3.1 Field Observations and Geochemistry

Sample site W2 (Fig. 2) was a small mound (~0.8 m high), which, upon inspection, turned out to be a disintegrating boulder, the composition of which was inferred to be andesitic because of its location. The boulder, W2, was the primary focus of this work because of the spatial differences in coloration and material properties (generally associated with depth into the boulder interior). Not only did it exhibit relief above the surrounding materials, it also appeared somewhat more cohesive than the other sample sites, which were soil-like, comprising easily

dislodged grains. As such, it was distinguishable from the surrounding altered mineral soil (Fig. 2B), a characteristic that would allow for identification of such a feature as a focused target for exploration on Mars within a generally habitable environment.

Temperature and pH changed from the surface of W2 to its interior (Table 2). The shallow surface was warm (36°- 47°C), but the temperature increased to 90°C in patches as little as 0.2 m depth below the surface. The pH increased from 1.06 near the surface to between 1.5 and 2.7 over the same interval (0.2 m). Colorful and differently textured cracks, presumably following original fractures allowing higher permeability were encountered within the disintegrating boulder. The surface was covered with white crystals in a dull, greenish, clay-like material. Below this, the material was more clay-rich with a buff to pink color. In some places at a depth of 1.0 to 2.0 mm, a thin (~ 1 mm), brilliant-green layer was observed (Fig. 2C, green layer labeled G). Below this, the material changed from buff to pink with depth. A 3.0 to 5.0 mm thick rust-colored horizon was observed in some places at a depth of 3.2 to 3.5 cm, but the layer was discontinuous. Occasional purple layers were also encountered, but their distribution was not systematic. The inhomogeneity inside the boulder points to a need to analyze multiple sites vertically and horizontally to select samples some of which may contain potential biosignatures.

Other samples consisted of gray-to-buff colored materials with some yellow crusts (W1, W4, WS5, WS8). The gray-to-buff materials comprise crystalline sand-sized grains with some clay material. The 'background' soil sample (W3), which was intended to be, but was not, a completely unaltered surface soil sample) consisted of light and dark colored sand- and finer-sized grains.

The carbon content of altered soils was very low, consistent with values reported for Solfatara Crater, Italy (< 0.6 wt%; Glamoclija et al., 2004). The carbon content for W2 was 0.69

wt% while the carbon content of W1 was 1.28 wt%. The carbon content of the background sample was considerably higher, i.e. 14.10 wt%. Both W1 and W2 were acidic soils with high silica content, and the concentrations of Si, Al, Fe, Ti, K, and Na, at both sites were depleted relative to the background site (W3, Table 2, S5), which corresponded to high concentrations of these ions in waters collected at the site (S4). We considered the possibility that some or all of the carbon was present as carbonate but ruled out that possibility for two reasons: no carbonate minerals were detected by any method (see below) and the low pH environment would dissolve carbonate minerals, which would be released as CO_2.

3.2 Mineralogy by Spectroscopy and Diffractometry

X-ray diffractometry (XRD) was performed on W1 and WS5 and on yellow subsamples of W2 and WS8 (Fig. 9-11). Mineral detections are shown in Table 3. The composition of crystalline phases in W1 comprised quartz and anatase (Table 3). Amorphous phases were not detected as indicated by the lack of a broad peak centered near d-spacing = 4.2Å (21°2Θ). Although samples from all sites contained quartz (SiO_2), the mineralogy of W2 and WS8 (Fig. 6,7) included jarosite and alunite, with distinct peaks for both minerals indicating they exist as separate phases. Peak positions were good matches to jarosite and alunite *sensu-stricto*, which are the potassium-end members of these minerals. Amorphous material was observed in XRD patterns of W2 and WS8, and levels could be as high as 80 % by Rietveld refinement and reference to an internal standard (4 wt% Si). In addition, WS8 also contained several other sulfate minerals including hydronium jarosite, ammoniojarosite, tschermigite, and carlsonite ($(NH_4)_5Fe^{3+}{}_3O(SO_4)_6 \cdot 7H_2O$); kaolinite ($Al_2(Si_2O_5)(OH)_4$) and clinoptilolite ($(Na/Ca)_{3-6}(Si_{30}Al_6)O_{72} \cdot 20H_2O$) were also identified. Quantification by Rietveld refinement failed for some

of these minerals and they are listed only as detected in Table 3. Sabieite ($(NH_4)Fe^{3+}(SO_4)_2$), carlsonite, and mohrite ($(NH_4)_2Fe(SO_4)_2 \cdot 6H_2O$) were present in small quantities as determined visually after applying a S/N of 3 to the first peak search but were not quantified possibly as a consequence of absent mineral intensity factors (e.g., Eberl, 2003). Other pink/buff/white material separated from the subsurface in W2 and from WS8 contained quartz along with amorphous materials but without any sulfate minerals (Table 3). These subsamples of W2 and WS8 were combinations of mechanically and chemically resistant quartz (100 wt%, data not shown).

The mineralogy by XRD of WS5 (Fig. 11) was different from that of W2 and contained some, but not all, minerals detected in WS8 (Table 3). In addition to quartz, which was common to all subsamples, WS5 contained the iron-sulfate salts, copiapite ($Fe^{2+}Fe^{3+}{}_4(SO_4)_6(OH)_2 \cdot 20H_2O$), sabieite ($(NH_4)Fe^{3+}(SO_4)_2$), and morhite ($(NH_4)_2Fe(SO_4)_2 \cdot 6H_2O$), but did not contain any alunite-group minerals. Both WS8 and WS5 contained tschermigite and clinoptilolite. Indeed, tschermigite was the most abundant mineral quantified in WS5 (Table 3). The presence of quartz (465 cm^{-1}) in these subsamples was confirmed by Raman spectroscopy (Fig. 5) in several subsamples of WS8 (WS8-yellow-1, WS8-yellow-2, WS8-yellow chunks, and WS8-buff samples). Strong ν_1 and ν_3 SO_4 peaks were observed in the ~1000 cm^{-1} region of the Raman spectra corresponding to alunite and jarosite bands, which were also observed by XRD. XRD confirmed that WS5 contained SO_4^{2-} minerals that were found nowhere else at WHS: sabieite ($(NH_4)Fe^{3+}(SO_4)_2$), morhite ($(NH_4)_2Fe(SO_4)_2 \cdot 6H_2O$), clairite ($((NH_4)_2Fe_3(SO_4)_4(OH)_3 \bullet 3H_2O$) and copiapite ($Fe(II)Fe(III)_4(SO_4)_6(OH)_2 \bullet 20(H_2O)$), which are all sulfate minerals that bear different cations for charge balance (Table 2, Fig. 6-8, S6) Clinoptilolite ($(Na,K,Ca)_{2-3}Al_3(Al,Si)_2Si_{13}O_{36} \bullet 12(H_2O)$) was found at both WS5 and WS8.

Mineralogy determined by VNIR spectroscopy revealed these and additional phases in samples collected at W2, WS5, and WS8 sites. Chips and particulate portions of material from WS8, exhibited VNIR spectral features consistent with tschermigite and Fe-NH_4-sulfate minerals, including bands due to water in polyhydrated sulfates near 1.45 and 1.94 μm such as hexahydrate, due to NH_4^+ near 1.56, 2.01 and 2.11 μm, and due to Al-OH in alunite near 2.17 μm. The VNIR spectrum of tschermigite (Meerdink et al., 2019; Sergeeva et al., 2019) includes strong water bands similar to those of hexahydrite as well as NH_4^+ bands related to those observed in spectra of other NH_4^+-minerals (Bishop et al., 2002; Berg et al., 2016). The broadness of the NIR tschermigite features near 1.48, 1.56, 1.79, 1.97, and 2.14 μm made it difficult to uniquely identify this mineral in mixtures, but our spectra of the WS5 and WS8 samples are consistent with the presence of tschermigite. Sulfate minerals were confirmed by Raman spectroscopy but could not be identified as jarosite, alunite, copiapite, or tschermigite. WS8 samples were heterogenous, with VNIR spectra of other WS8 subsamples showing a narrow band near 1.41 μm attributed to Al-OH and bound water in montmorillonite or zeolites such as clinoptilolite, a narrow band at 1.91 μm due to bound water in montmorillonite or zeolites, as well as a broad band near 1.95 μm that is characteristic of water in hydrated sulfates. An additional broad band near 2.2-2.3 μm is consistent with a synthetic, amorphous phase similar to Fe-rich opal (Fig. 9A).

The spectrum of the W2B particulate subsample contained weak features near 1.47 and 2.26 μm that are consistent with a small amount of jarosite and a weak band at 2.21 μm that could indicate some montmorillonite or kaolinite in this sample. Yellow jarosite crystals in some of the samples contained distinctive VNIR spectral features due to jarosite at 1.47, 1.86, 2.22, and 2.26 μm (Fig. 9b). One such subsample from WS8 also included water bands near 1.42 and

1.94 μm that are consistent with hydronium jarosite or a hydrated material in this sample. Accompanying W2 particulates and light orange chunks exhibited VNIR spectral features consistent with jarosite, alunite, and tschermigite, including bands due to water in polyhydrated sulfates near 1.45-1.48 and 1.94-1.98 μm, due to NH_4^+ near 1.56, 2.01 and 2.11 μm, and due to alunite near 2.17 μm.

The WS5 samples exhibited VNIR spectral features consistent with tschermigite, including bands due to water in polyhydrated sulfates near 1.45-1.48 and 1.94-1.98 μm, due to NH_4^+ near 1.56, 2.01, and 2.11 μm, and due to Al-OH in alunite near 2.17 μm. The particulate WS5 spectrum also had weak bands at 1.41 and 2.21 μm that were attributed to kaolinite, as that is also consistent with the XRD results. The WS5 chunk spectrum contained features consistent with Fe in copiapite at 0.43 and 0.89 μm as well as broad water bands near 1.4 and 1.9 μm. Copiapite was also identified in XRD analyses of WS5. Mineral suites identified by VNIR spectroscopy and XRD overlapped but were not identical.

3.3 Spatially Resolved Mass Spectrometry and Raman Spectroscopy

A mineral soil sample, W1, produced GALDI-FTMS patterns expected for organic-poor, Al-bearing silicate-rich soil weathered from andesitic country rock (Fig. 3; K, Ca, Fe, Ti, Ba). Additional peaks with mass defects distinctive of inorganic elements and with indeterminate mass defects (see below) were observed (Table 4). GALDI-FTMS analysis of W1 showed mainly inorganic mass peaks (Fig. 3, S8). Individual cations are detectable as singly charged ions (S3) and were observed; K^+ and Ca^+ were consistently observed and are considered background ions (Fig. 3), S7). Fe^+ was observed with Ca^+ but not with K^+ in W1 (Fig. 3a). This suggested that the Fe^+ was not associated with K^+, which would be diagnostic for jarosite.

While peaks at m/z 428.787 and 448.839 (Fig. 3c) may look as though they have isotopic patterns (M, M+1, and M+2) consistent with hydrocarbons, their mass defects reveal that they originated from Al-bearing silicates corresponding to $Al_5Si_3O_{13}H_2^+$ and $Al_7SiO_{14}H_8^+$, respectively. Another typical pattern observed for Al-bearing silicate-related peaks is illustrated in Fig. 3d with m/z 472.708 assigned to composition $Al_5Si_5O_4S_4H_6^+$.

In W2, spectral peaks with mass defects indicative of inorganic species had little similarity to those of W1 (Table 4). The majority of laser shots in W2 documented the presence of K^+ and Fe^+(Fig. 4, bkgd, S7a, S8), which are diagnostic for jarosite when seen together (Kotler et al., 2008). Inorganic ions reflecting Al-bearing silicate signatures were found in W1 but not in W2 while signatures of jarosite were found in W2 but not W1 in over 100 laser shots.

W1 produced some spectra with peaks that have mass defects indicating the presence of significant carbon and hydrogen (Fig. 3e). The peaks at m/z 438.491 and 201.221 were assigned compositions $C_{29}H_{62}N_2^+$ and $C_{13}H_{31}N^+$, respectively. Higher mass peaks around m/z 2035, 3900, and 4150 (Fig. 3f) are also likely to be organic in origin because very high mass peaks (>2000 amu) are not common with laser desorption of inorganic compounds and have not been observed with pure minerals in our laboratory. Consequently, we can report that organic compounds were detected in W1 by GALDI-FTMS, that some of these organic compounds were of high molecular mass (i.e. > 2000 u), and that laser shots with organic species covered a smaller area of the grid than those without organic species.

Further, Al-bearing silicate-related spectral peaks, examples of which were seen in W1, were not identified in W2 (Table 4). W2 appeared to have more peaks with mass defects consistent with organic species than did W1 (S8), and high-mass peaks (>2000 u) were seen over a greater proportion of the grid in W2 (Fig. 4a) than in W1 (Fig. 3a). In addition, there were

lower mass peaks in the W2 sample at m/z 319.107 and 371.139 (Fig. 4b) that had mass defects consistent with organic species $C_{14}H_{25}O_3K_2^+$ and $C_{18}H_{29}O_3K_2^+$, respectively, that were not found in W1. In other spectra (not shown), a peak at m/z 318.869 and its isotopes obscured the peak at m/z 319.107, and the latter's presence could not always be confirmed. Also, there were some very high mass peaks around m/z 6600 (not shown) in W2 that are not seen in W1. Compositions for these peaks were not assigned because they were not isotopically resolved with the FTMS parameters used to survey these samples, but the peaks are likely organic for the reasons given above. In a separate survey of W2, another peak (315.253 m/z) was identified as $C_{16}H_{38}NO_2K^+$ (S7b). This peak was found in conjunction with diagnostic peaks for jarosite (K^+ and Fe^+) (S7a).

Raman spectroscopy confirmed the presence of organic compounds in samples from W2 as well as from WS8 (Fig. 5A) and W5 (data not shown). Suspected broad organic combination bands (C, C=C, C=N) were observed in the 1200+ cm^{-1} region, particularly for the WS8 samples. The overall spectral baseline was red-shifted, supporting the presence of fluorescence due to organic compounds. One spot on the WS8 sample exhibited Raman bands near 1230, 1320, 1610, and 1690 cm^{-1}. The 1230 cm^{-1} band is consistent with sp^2 type bonds such as those found in aromatics or graphite. The band at 1320 cm^{-1} is consistent with the carbon D band of carbonaceous materials (Wopenka and Pasteris, 1993; Beyssac et al., 2003). Bands at 1610 and 1690 cm^{-1} are C-C related functional groups in rings and polymeric chains with O atoms in the structure (Kaiser Optical Systems, 2018). Fig. 5B demonstrates that higher concentrations of organic matter were observed in yellow subsamples of WS8 than in buff subsamples. WS8-yellow-1 exhibited organic fluorescence and Raman bands in the 1200-1800 cm^{-1} region with 1219 and 1311 cm^{-1} corresponding to ring vibrations or CH_2 and in-plane CH deformation, respectively. The band at 1605 cm^{-1} could be assigned to NH_2. WS8-buff exhibited jarosite peaks

at 1009, 1103, and 1147-1154 cm^{-1} due to the SO_4 symmetric and asymmetric stretching modes (Sasaki et al., 1998; Frost et al. 2006), related alunite SO_4 peaks at 1027-1036 cm^{-1}, and possibly a tschermigite SO_4 peak at 994 cm^{-1}. Greater fluorescence baselines and combination Raman bands were observed in WS8-yellow-1 compared to WS8-buff indicating a higher concentration of organic compounds in WS8-yellow subsamples (Fig. 5a).

4 Discussion

Washburn Hot Spring samples showed linkages between geochemistry and mineralogy that help delineate targets within larger areas as analogs for exploration of potential habitable environments or biosignatures on Mars. The application of several analytical techniques showed similarities and differences in the minerals detected, along with the presence, absence, and type of organic compounds observed (S1). Although all techniques were more or less capable of identifying minerals (except for tschermigite, copiapite, and hydrated Fe-NH_4-sulfate minerals), GALDI-FTMS and Raman spectroscopy also detected organic matter. And among detections by GALDI-FTMS, the sample with jarosite (W2) exhibited more diverse organic compounds (as identified by more numerous peaks with mass defects indicative of organic matter) than did the Al-bearing silicate sample (W1), and organic matter was more frequently observed in the map of W2 (Fig. 4) than in the map of W1 (Fig. 3).

The surface of the WHS study site is covered with a sugary white crust containing quartz crystals weathered from igneous minerals in the andesitic country rock. Among the sites, W2 showed distinctive relief, which would aid in autonomous target selection, coupled with geochemical, thermal, and visual zonation (pH, temperature, mineralogy, and coloration) along with distinctive mineral-organic associations. The green coloring of the thin horizon below the

surface of W2 is almost certainly caused by the photosynthetic pigments of *Cyanidium caldarium* , as this microbe was shown to be present in W2 using DNA-based techniques (data not shown, Henneberger, 2008). This eukaryote is commonly found in acidic, thermal soils, around hot spring and/or acid-sulfur vents, forming such green-colored surface layers (Ciniglia *et al*., 2004; Pinto *et al*., 2003). Although not identified as pigments, the red shift observed by Raman spectroscopy supports this interpretation.

In this study, organic matter was more readily detected by GALDI-FTMS when associated with jarosite than with Al-bearing silicates. However, organic matter was detected by Raman spectroscopy at all sites. Salts, in general, are excellent matrices for laser desorption and ionization of organic matter; salts are able to ionize organic species by cation attachment. Al-bearing silicates have variable abilities to ionize organic matter. Among the sites, therefore, W2 represents a good target for the search for potential biosignatures, especially when found in specific combination with organic-rich Al-bearing silicate materials such as W1. Importantly, specific combinations of instruments are needed to detect potential biosignatures when targeting these sites. The characteristics of W2 can be used as a template for how to effectively sample on Mars.

4.1 Mineralogy and Geochemistry

The andesitic country rock is the source of the major elements found in the mineral soils and crusts at WHS. Feeley et al. (2002) report petrologic zonation of the andesite lava from basaltic-andesite in the southwest quadrant across the Grand Loop Road from WHS, K-rich andesite in the south-central portion, and dacitic-andesite along the northern and eastern quadrants of Mt. Washburn. By extrapolation from Fig. 2 in Feeley et al. (2002), WHS lies

within the K-rich andesite zone or at least near its margin with the basaltic-andesite of the southwestern quadrant. Modal analysis of samples from the K-rich andesite collected near WHS comprise plagioclase>clinopyroxene>orthopyroxene>olivine>Fe-Ti oxides. Quartz, amphibole, and biotite were not present in the modal suite of the K-rich andesite but were present in that of the basaltic-andesite (Feeley et al., 2002). The Fe,Mg- and Al-bearing silicate minerals (e.g., olivine (Fo_{85}-Fo_{72}), pyroxene (cpx $Wo_{34-36}En_{43-52}F_{5-16}$; opx $Wo_{2-5}En_{67-81}Fs_{16-30}$), plagioclase ($An_{83}$-$An_{40}$), Feeley et al., 2002) chemically weather under acidic conditions to mobilize major elements taken up in metastable and clay minerals (Eq. 1-4). Dissolved Si can precipitate as quartz or can combine with Al to form kaolinite ($Al_2Si_2O_5(OH)_4$). Although quartz is found at all sites, kaolinite is identified (XRD) at only one site: WS8. Its absence at other sites may be a consequence of lower pH and higher temperature values found elsewhere. It is also possible that the crystal size was below the resolution by XRD or that the concentration was below the detection limit at these other sites.

The breakdown of Fe-Mg- and Al-bearing silicate minerals also releases the cations (e.g., Mg^{2+}, K^+, Ca^{2+}) in the crusts of efflorescent minerals (Eqs. 1-4).

(1) $NaCaAl_3Si_5O_{16} + 5.5H_2O + 3H^+ = Ca^{2+} + Na^+ + 2H_4SiO_4 + 1.5Al_2Si_2O_5(OH)_4$ (derived from Arnórsson and Stefánsson, 1999)

(2) $Na_{0.5}Ca_2(Fe_{1.3}Mg_{2.6}Al_{1.1})(Al_{1.6}Si_{6.4})O_{22}(OH)_2 + 15H^+ + H_2O = 0.5\ Na^+ + 2Ca^{2+} + 2.6Mg^{2+} + 1.3Fe^{2+} + 2.7\ Al(OH)_3 + 6.4\ H_4SiO_{4(aq)}$ (Velbel,1989)

(3) $MgSiO_3 + 2H^+ = Mg^{2+} + SiO_2(aq) + H_2O$ (adapted from Oelkers and Schott, 2001)

(4) $MgCaSi_2O_6 + 4H^+ = Mg^{2+} + Ca^{2+} = 2SiO_2 + 2H_2O$ (modified from Murphy and Helgeson, 1987)

Fe(II) in amphibole, olivine, and iron oxides oxidizes to Fe(III), leading to precipitation of Fe(III) minerals (Eq. 5), which are observed at W2. Oxidation of reduced S species to SO_4^{2-} most likely occurs in this same zone (Eq. 6). Alternatively, direct oxidation of sulfide in pyrite (FeS_2) by Fe(III) leads to formation of acidic, Fe(II)-SO_4^{2-} systems (Eq. 7). In Yellowstone thermal systems, S is found mainly as sulfide or elemental sulfur until oxidized to sulfate at or near the surface. Given Fournier's (1989) interpretation that at WHS ammonia emanates from marine sediments heated at depth by volcanism, it is reasonable that $H_2S_{(g)}$ would have a similar source. In addition to sulfide minerals (e.g., pyrite), sulfur is present in marine sediments as organic sulfur. Minerals and organic matter are the likely sources of sulfur species in the fumaroles of WHS, although it is possible that some sulfate derives directly from evaporation of infiltrated meteoritic water, as does most of the dissolved chloride found in thermal areas elsewhere in Yellowstone (Fournier, 1989). In the presence of cations released from country rock during weathering, Al^{3+} or Fe(III) and SO_4^{2-} precipitate together to form alunite, jarosite, and copiapite, which were identified in this study (Eqs. 8,9,10). Copiapite is a mixed redox state Fe-bearing mineral, indicating ongoing oxidation weathering processes.

(5) $Fe^{2+} + (5/2)H_2O + ¼\ O_2 = Fe(OH)_3(s) + 2H^+$ (Nordstrom, 1989)

(6) $H_2S + 2O_2 = H_2SO_4$

(7) $FeS_{2(s)} + 14Fe^{3+} + 8H_2O = 15\ Fe^{2+} + 2SO_4^{2-} + 16\ H^+$ (Nordstom , 1989)

(8) $KAl_3(SO_4)_2(OH)_6 + 6H^+ = K^+ + 3Al^{3+} + 2SO_4^{2-} + 6H_2O$

(9) $KFe_3(SO_4)_2(OH)_6 = K^+ + 3Fe^{3+} + 2SO_4^{2-} + 6H_2O$

(10) $5FeSO_4.7H_2O + O_2 + H_2SO_4 = Fe^{2+}Fe^{3+}{}_4(SO_4)_6(OH)_2 \bullet 20H_2O + 15\ H_2O$ (, 1989)

The combination of andesite with volcanic gases (e.g., H_2S) leads to a mineral suite comprising more stable Al-bearing silicate minerals or quartz and sulfate salts. The sulfate salts

observed at WHS are found in caves and fumaroles associated with volcanism (Rodgers et al., 2000; Košek et al., 2017; McHenry et al., 2017) and in burning coalmine dumps (Kruszewski, 2013; Košek et al., 2017; Shimobayashi et al. (2011)). It seems unlikely that coal beds exist on Mars, but fumaroles and hot springs have been suggested as good targets to explore for potential biosignatures (McHenry et al., 2017; Cady et al., 2018a)

The relief of the disintegrating boulder enabled visual identification of a promising target, which led us to excavate and sample the subsurface exposing ephemeral and efflorescent phases. Selective sampling of yellow, brown, and green materials from within the W2 site yielded localized concentrates of jarosite (Eq. 10) along with alunite (Eq. 8), both of which have been identified on Mars (alunite: Ehlmann et al., 2016; Baldridge et al., 2014; Swayze et al. 2008; Sessa et al., 2018; jarosite: Madden et al. 2004; Klingelhofer et al., 2004; Morris et al., 2006; Farrand et al., 2009; Ehlmann and Mustard, 2012; Bishop et al., 2018). Alunite (Eq. 9) is the surface expression of low-sulfidation mineralization as a consequence of near-neutral meteoric water infiltration near a deep-seated heat source (Rye, 2005). Jarosite is also found in such systems, but it forms under lower pH and more oxidizing conditions (Blahd, 1982; Stoffregren, 1993) and almost always replaces alunite when the two are found together (Rye, 2005; Papike et al., 2006). We could not confirm whether jarosite was replacing alunite, but replacement could not be ruled out. In any case, the simultaneous occurrence of alunite and jarosite illustrated an evolution of the Washburn system from a less to more oxidized and acidic system. Chemical weathering was nearly complete at greater depth in W2 and in W1, leaving only quartz, anatase (W1) and amorphous materials behind; not even clay minerals were detected in the highly altered samples, similar to observations of acid alteration at Rio Tinto (Mavris et al., 2018). The loose quartz crystals comprising the sugary crust are puzzling because no quartz is calculated in the

modal analysis of either the high-K or basaltic-andesite. Several equations (Eqs. 1-5) point towards formation of quartz directly from dissolved SiO_2. However, it is possible that quartz was present in some rocks in this area and weathered out to form the crystals on the surface.

McHenry et al. (2017) observed ephemeral NH_4-bearing minerals (tschermigite and lonecreekite ($(NH_4)Fe(SO_4)_2 \cdot 12(H_2O)$) in deposits formed around fumaroles and hot springs of Mt. Lassen, CA, USA. The source of the ammonia was not identified but could be organic matter released from baked sediments under the Cascade subduction zone, similar to the sedimentary source of ammonia at WHS. This may also be the case in Ruatapu Cave (Rodgers et al., 2004) where tschermigite was tentatively identified. Ruatapu Cave is on the North Island of New Zealand, which comprises, for the most part, a volcanic island arc associated with the Kermadec-Tonga trench. The Fe and NH_4-bearing sulfate minerals have different amounts of associated water molecules. It is likely that additional Fe-NH_4-bearing sulfate minerals could also form sometimes at WHS or that the minerals identified here might not be detected at other times depending on the relative humidity as was observed at Lassen Volcanic National Park (McHenry et al., 2017).

Tschermigite, a member of the alum group, and sabieite, an ephemeral NH_4-Fe-sulfate mineral, were identified in WS5, along with copiapite, clinoptilolite, and quartz. This assemblage differs from that found in Lassen fumaroles and hot springs (McHenry et al., 2017). These researchers observed a greater number of efflorescent Al-, Fe(II)-, Fe(III)-, Ca-, Mg- and mixed-cation sulfate minerals. Copiapite and other Fe-sulfate minerals observed at WS8 were not observed at Lassen; indeed, only a few Fe(II)-sulfate minerals were observed at Lassen. The authors note that the conditions and mineral assemblages varied from year to year probably as a consequence of variable temperature, desiccation, and precipitation. Further, they observed more

silica minerals (opal, quartz, tridymite, and cristobalite) along with iron sulfide minerals and iron or titanium oxide minerals. Tschermigite was observed twice, both times associated with mineral crusts. Lassen is an active volcanic system and a more complex one than is Mt. Washburn (55-52 ma). Variable redox and meteorological conditions likely contributed to the greater diversity of sulfate and silica minerals, and to the presence of sulfide and oxide minerals. Tshermigite is also observed as an efflorescent mineral in caves. The caves are formed by large vents that release steam and sulfidic gases (Rodgers et al., 2000; Audra and Hoblea, 2007). Audra and Hoblea (2007) found aluminum sulfate minerals growing on the side of an aluminum-framed glass so the occurrence is not entirely natural. Burning coal-mining dumps are other examples of unnatural occurrences (Kruszewski, 2013). The heat and presence of sulfide minerals and organic sulfur are similar to the subsurface environment proposed for Mt. Washburn. That is, the modern Yellowstone volcano provides the heat, which bakes the underlying marine sediments leading to release of ammonia and sulfide.

The WS5 site, which was lower than the other sites, offered a view of an earlier stage in the development of Washburn Hot Springs in that the mineral suite there contained examples of less oxidized minerals, including tschermigite (Eq. 10) and copiapite (Eq. 9). Tschermigite is an ephemeral mineral that easily dissolves in water. Its presence suggests tschermigite formed quickly after a rain event; the area had experienced no significant recent rainfall at the time of sampling; 6.0 mm of rain fell at the National Atmospheric Deposition Program (NAPD) site closest to Washburn Hot springs, Yellowstone National Park - Tower Falls (WY08), in the week prior to sample collection (NADP, http://nadp.sws.uiuc.edu/).

Ammoniojarosite was expected at the Washburn site because of the high ammonium content reported by others (Fournier, 1989; Spear et al., 2005) and was only observed at WS8,

possibly due to the stability of the thermodynamically favored K-bearing jarosite phase. Other ephemeral ammonium-bearing minerals were detected: mohrite, tschermigite, sabiete and possibly, clarite. These phases offer a means of trapping ammonium and therefore may be relevant in nitrogen cycling as a solid reservoir in acidic, thermal soils. The ammonium signature in tschermigite was visible in VNIR spectra and distinguishable from the ammonium signatures of ammonium-bearing clay minerals and ammonium alunite, which were not detected (Fig 6). In general, WS5 was less chemically weathered than other sites as demonstrated by the presence of metastable minerals such as the zeolite clinoptilolite. Clinoptilolite forms as an authigenic or diagenetic mineral in marine sediments, particularly those with high silica and K^+ content (Nathan and Flexer, 1977; Bohrmann et al., 1989). Clinoptilolite, found at WS5, is known to absorb ammonia from wastewater (Du et al., 2005; Ji et al., 2007) and may provide another source of fixed nitrogen. Ammonia-bearing minerals could provide fixed nitrogen (tschermigite and clinoptilolite) and mixed redox state iron-bearing minerals (copiapite) that could support microbial communities in this habitat.

4.2 Detectability of Organic Matter in a Given Mineral Matrix

Chemistry and mineralogy affected our ability to detect organic compounds by GALDI-FTMS because the minerals can essentially act as a geomatrix to help desorb and ionize the organic compounds. Jarosite minerals provide good substrates for desorption and ionization of associated organic compounds (Kotler et al., 2008). Indeed, in our study, organic compounds were more frequently detected by GALDI-FTMS and had greater compositional variability in W2, which contained jarosite, than in W1, which was dominantly Al-bearing silicate, despite lower organic carbon content in W2 than in W1 (Table 2). The GALDI-FTMS signature for

jarosite was not detected at W1, where predominantly inorganic Al-bearing silicate compounds were detected (Fig. 3A). Further, only a few locations demonstrated peaks with organic mass defects in W1 (Fig. 3E). Most of the inorganic species were Ca-bearing material, which is interesting because no Ca-bearing phases were detected by XRD; GALDI-FTMS detects phases, elements, and compounds that are easily desorbed and ionized (e.g., Ca) but that are not necessarily the most abundant phases (Yan et al., 2006). Ti- and Ba- bearing materials and Al-bearing silicates were also detected. One fragment with composition $Al_5Si_5O_4S_4H_6^+$ was the only S-bearing phase identified. This fragment likely formed in the GALDI-FTMS in the gas phase by attachment or incorporation of S with the ion given that sulfur and oxygen exchanges have been observed in the gas phase (Groenewold et al. 2001). Additionally, K and Fe were observed but never in the same W1 spectrum as they would be if together in jarosite. Both are components of jarosite but are usually detected by GALDI-FTMS together when jarosite is present (Kotler et al., 2008). Further, although jarosite was detected in other samples by XRD, it was not detected in W1, either because its concentration is below detection by XRD (3-5 wt%) or the crystal size is below the resolution by XRD. Consequently, we conclude that jarosite, if present in W1, occurred at very low concentrations. Anatase, identified in W1, is the likely source of Ti species observed by GALDI-FTMS. The GALDI-FTMS spectra, therefore, suggest the mineral matrix of W1 comprises Al-, S-, K-, and Fe-bearing silicates and oxide minerals such as anatase. With the exception of Fe-bearing minerals, minerals containing the other components were confirmed by XRD.

4.3 GALDI-FTMS Detection of Organic Compounds and Minerals

The differences in the number of detections and the diversity of organic compounds detected by GALDI-FTMS in Washburn Hot Springs samples may be explained by the matrix composition. The difference between the two matrices was the presence of jarosite in XRD patterns and the co-occurrence of K^+ and Fe^+ in GALDI-FTMS spectra in W2. Several of the organic peaks that were identified (e.g., $C_{14}H_{25}O_3K_2^+$, $C_{18}H_{29}O_3K_2^+$, and $C_{16}H_{33}O(NH_3)(H_2O)K^+$; S.I.3) may represent fatty acids because of the C:H ratio of close to 1:2. One of the fatty acid candidates was detected in W2 coincident with the mineral signature (K^+ and Fe^+) for jarosite (SI 8). Minerals with alkali metals and SO_4^{2-} (e.g., jarosite and thenardite) have been shown to aid detection of organic compounds in natural samples (Kotler et al., 2008; Richardson et al., 2008). It is possible that association with jarosite helps preserve organic matter as well, but because jarosite is a secondary mineral, the ages of the natural samples studied by Kotler et al. (2008), and in which they found organic species, are unknown and therefore may be quite young. The minerals, though, remain good targets for rapid and high-resolution detection of organic compounds by GALDI-FTMS. An environment similar to that of W2 with favorable mineralogy would be an excellent target to detect organic compounds, some of which may be potential biosignatures.

The importance of the GALDI-FTMS results is underscored by the relative abundance of phyllosilicate and sulfate co-occurrences on Mars. Phyllosilicates are the most common hydrous mineral detected on Mars with sulfates, zeolites, and salts present in significantly lower abundance (Carter et al., 2013). Yet as targets for exploration, sulfates present an opportunity for easier detection of organic matter where present. This supports exploring paleolake areas within Gale and Jezero craters on Mars that contain sulfates in addition to clay minerals. Indeed, an

environment that combines the preservation potential associated with phyllosilicate minerals and the efficiency of desorption and ionization provided by salt minerals might be the best candidate.

The masses observed by GALDI-FTMS could be molecular ions, ion fragments of larger molecules, or ions produced in the gas phase during the laser-desorption process. Therefore, the C:H ratios close to 1:2 do not provide definitive evidence that fatty acids are present but rather that they may occur in the sample. Although GALDI-FTMS detected organic compounds at both W1 and W2, a greater diversity of organic compounds, as indicated by mass defects illustrative of organic matter, was more frequently detected in laser shots in W2 than in W1. The GALDI-FTMS parameters in this study could not distinguish branching or other structural properties, and therefore cannot be used to determine the origin of the potential fatty acids despite reported differences in archaeal and bacterial fatty acid composition. Archaeal fatty acids include carbon chains of 20 or more atoms as branched alkyl chains, which may be more resistant to oxidation (Leman, 2009). On the other hand, bacterial fatty acids generally contain fewer carbon atoms and are not branched. In the future, GALDI-FTMS parameters for MS^n techniques could potentially determine such structural differences by examining induced fragmentation patterns of a selected parent compound. Nevertheless, in this study, the greater diversity of organic compounds at W2 than at W1 may result from greater microbial diversity at W2 or from better detectability of organic matter in jarosite than in Al-bearing silicates; diversity and organic carbon content are inversely related.

For the most part, VNIR (mineralogy) and Raman spectroscopy (mineralogy and organic matter) results agreed with those of XRD (mineralogy) and GALDI-FTMS (inorganic chemistry and organic detection frequency and diversity). Organic matter was detected by Raman spectroscopy and by GALDI-FTMS. Yet the frequency of detection and the diversity of

compounds by GALDI-FTMS were greater and the abundance of organic matter by Raman spectroscopy and bulk carbon content was lower in the disintegrating boulder (W2) than in W1. This finding is significant because VNIR and Raman spectroscopy are easily applied to *in situ* environmental scans of a selected area; both can quickly identify promising areas for further analysis or for sample collection; VNIR from orbit or the surface, and Raman from the surface.

Detection limits for Raman, VNIR, and other forms of spectroscopy depend on the sensitivity of the mineral absorptions and the type of spectrometer. Raman spectroscopy measures fundamental stretching and bending vibrations of molecular groups in the mineral structure (e.g., Sharma and Egan, 2019), similar to mid-IR spectroscopy (e.g., Lane and Bishop, 2019); however, only Raman "active" and IR "active" vibrations are detected by each technique, depending on group theory. Raman active modes include a change in the polarizability of the molecule during vibration, while IR active modes have a change in the dipole moment during vibration. VNIR spectroscopy measures combinations and overtones of these fundamental vibrations (e.g., Bishop, 2019). In general, Raman spectroscopy has a lower detection limit (100 ppm; Sobron et al., 2014) than does VNIR spectroscopy; Lanzarotta (2015) report detection limits of 100s to 1,000s of ppm depending on particle size while Ye and Glotch (2016) report detection limits for minor minerals in chloride-mineral mixtures to be in the one to 10s of percent range. Other studies have shown detection of clay minerals in mixtures at a few percent using VNIR spectra of mixtures (e.g., Bishop et al., 2013; Stack and Milliken, 2015; Robertson and Milliken, 2016). Detection and characterization of clay minerals by Raman is more challenging because of scattering of the small particles (e.g., Bishop and Murad, 2004), but Raman signals for clay minerals and other fine-grained components can be strengthened by pressing the samples into pellets (e.g., Wang et al., 2015). Raman detection of sulfate vibrations is often better than

VNIR, but Fe-bearing minerals are better detected by VNIR because Fe excitations can be detected as well as molecular vibrations (e.g., Sobron et al., 2014). Raman also has the advantage of investigating spot sizes on the order of a few microns, which enables detection and characterization of minor components in samples.

Because vibrations of molecules are detected with Raman and VNIR spectroscopy, both of these techniques are more sensitive to minor mineral phases than is XRD. Conversely, XRD consistently detects all crystalline minerals at a few percent abundance (e.g., Chipera and Bish, 2013; Eberl, 2003). Raman spectroscopy complements VNIR spectroscopy for detection of molecular groups in minerals. VNIR spectroscopy is particularly successful at detecting the species observed in hydrous phases, ammonium phases, metal- hydroxide phases, and Fe-bearing materials. The exact locations of the bands are tied to the crystal structure and type of cation in distinct minerals, although the interpretation is not always unique. Clay minerals and Al-bearing silicate minerals are more easily detected with VNIR spectroscopy than with Raman spectroscopy. The Raman spectra presented here showed numerous sulfate bands, but the minerals were indistinguishable in these mixtures. Combining these two techniques offers a superior representation of the types of phases present and each is more sensitive than XRD for poorly crystalline phases. Raman also has the advantage that it can detect vibrations in hydrocarbons and other organic components.

Compared to XRD mineralogy and GALDI-FTMS chemistry, VNIR spectroscopy identified the same (and additional) minerals in W2 compared to W1. Raman results confirmed the presence of quartz at WHS. Raman spectroscopy further confirmed the presence of organic matter in the Washburn samples and confirmed that organic matter was more diverse and more frequently detected in the samples that contain sulfates than in those that did not. This is

significant if laser desorption will be used to probe acidic environments; sulfate minerals are a better substrate for laser desorption than are clay minerals alone for detection of identifiable organic matter, i.e. possible biosignatures, than Al-bearing silicates even though the organic carbon content is higher in the latter matrix. The presence of both groups of minerals together is promising for detecting organic matter. The laser desorption ionization complements the pyrolysis and the derivatization methods of sample introduction for MOMA. These three sample introduction methods are included in the MOMA instrument in the ExoMars payload (Goetz et al., 2016). Future exploration of Mars should consider the origin and not just the presence of clay minerals in identifying targets for exploration. If clay minerals are of hydrothermal origin, they may be good targets because of the presence of jarosite (or other salts).

5 Implications

Taken together, these observations suggest that within a given area or among different prospective samples, those with chemical, spectral, or mineralogical signatures for jarosite would be good candidates for detection of organic molecules because of the effectiveness of jarosite in promoting detection of organic compounds; salts, in general, amplify the signals of organic materials (Kotler et al., 2008; Richardson et al., 2008; Yan et al., 2007a,b). These results contrast with the conclusions of Lewis et al. (2015) who propose that the current method for detecting organic compounds in use on Mars reduces the likelihood of finding organic compounds associated with sulfate minerals. The current method introduces the sample to the mass spectrometer by pyrolysis, which is a different method than laser desorption. Pyrolysis decomposes sulfate, which subsequently reacts with organic compounds during analysis. Gordon and Sephton (2016) confirm these concerns when they reported that indeed, sulfate reacted with

organic matter in pyrolysis experiments. The method of sample introduction clearly matters, and these results highlight the need for balance between the ability to store and protect organic matter, which is attributed to clay minerals over jarosite, and the ability to aid in location and detection of organic matter, which could be attributed to jarosite over clay minerals. These observations underscore the importance of selecting the analytical technique to match the requirements of detection in specific environments and suggest the need for continued field investigation of jarosite-bearing environments as potential Mars analog sites. The heterogeneous and low-density distribution of organic compounds in Al-bearing silicate-bearing W1 contrasted with that of jarosite-bearing W2. Consequently, exploration should consider analog environmental conditions and mineral combinations to direct sampling for organic compounds.

Our study of several samples from the Washburn Hot Springs at Yellowstone National Park confirmed that jarosite is a good target for detecting organic compounds. The results presented here support the hypothesis that detection of jarosite at sites on Mars could be used to identify potential targets for life detection. First, more numerous and diverse organic compounds were detected by GALDI-FTMS in samples with elevated jarosite abundance than in those dominated by the Al-bearing silicates, although organic matter was detected in samples with and without jarosite by Raman spectroscopy. Because Al-bearing silicates are considered better for preserving biosignatures (Summons et al., 2011), we propose focusing on sites that contain both jarosite and Al-bearing silicates as favorable for retention (Al-bearing silicate strength) and detection (jarosite strength) of organic compounds that may be biosignatures. Second, organic compounds detected in the absence of jarosite were not as diverse as those found in its presence. These results further support our previous work (Kotler et al., 2008, 2010) focusing on jarosite as a target mineral for the search for life on Mars because it promotes detection of organic

compounds that could be biologically derived. Our GALDI-FTMS and Raman spectroscopy results demonstrated that in thermal areas, localized salt deposits provide greater opportunities for detection of organic compounds than do phyllosilicates, despite having lower organic carbon contents. Regions of phyllosilicate dominance and jarosite dominance are visible in thermal areas on a meter scale in our study. VNIR spectral analyses identified jarosite and associated minerals in our samples, suggesting that these could be detected on the surface of Mars by a rover carrying a VNIR spectrometer.

VNIR spectroscopy is a first step in studies of the surface mineralogy of Earth and other planets because VNIR spectra can be collected from orbit. Raman spectroscopy, on the other hand, requires closer proximity. It is important, therefore, to understand how the two spectroscopic methods complement each other by ground-truthing their results with XRD, the definitive mineralogical technique. These tools, along with GALDI-FTMS, provided a comprehensive view of the mineralogical, chemical, and textural variability in a complex geological system related to clay- and sulfate-bearing outcrops on Mars.. The results of our hydrothermal analog study showed that identification of jarosite-bearing sites initially from orbit by CRISM and then by SHERLOC on the surface can provide information on potentially productive habitats to search for organic matter and evidence of life at the time the jarosite formed.

6 Acknowledgements

RMH was funded by Macquarie University (Postgraduate Research Fund and an International Travel Scholarship). NWH, JRS, CDR, and JMK were funded by the National Aeronautics and Space Administration (NASA) Exobiology Program (Grant No.

NNX08AP59G). NWH, VCG, and JLB received funding from the NASA Astrobiology Institute (Grant No. NNX15BB01A, N. Cabrol, PI). JLB also received support from the NASA MDAP program (Grant No. NSSC19K1230). PM was a NASA Intern at NASA ARC funded by the California Space Grant under the mentorship of VCG. GB was a NASA Graduate Student Intern at NASA ARC funded by the USRA under the mentorship of VCG. VCG, PM, and GB thank Dr. Job Bello (Spectra Solutions, Inc.) for the dual excitation probe EIC Raman Instrument. NWH thanks Gretchen Grimes for assistance. Research was performed at the Idaho National Laboratory under DOE Idaho Operations Office Contract DE-AC07-05ID14517. Research in Yellowstone National Park was conducted under research permit YELL-SCI-1660.

Author Disclosure Statement

No competing financial interests exist.

7 References

Alpers, C.N., Nordstrom, D.K., and Ball, J.W. (1989) Solubility of jarosite solid solutions precipitated from acid mine water, Iron Mountain, California, USA. Sciences Geologiques Bulletin, 42, 281-298.

Arnorsson, S., and Stefansson, A. (1999) Assessment of feldspar solubility constants in water in the range 0 degrees to 350 degrees C at vapor saturation pressures. American Journal of Science, 299(3), 173-209.

Audra, P., and Hoblea, F. (2007) The first cave occurrence of jurbanite Ai(OH SO4) center dot 5H(2)O , associated with alunogen Al-2(SO4)(3) center dot 17H(2)O and tschermigite NH4Al(SO4)(2) center dot 12H(2)O : Thermal-sulfidic Serpents Cave, France. Journal of Cave and Karst Studies, 69(2), 243-249.

Baldridge, A., Hook, S., Crowley, J., Marion, G., Kargel, J., Michalski, J., Thomson, B., de Souza Filho, C., Bridges, N., and Brown, A. (2009) Contemporaneous deposition of phyllosilicates and sulfates: Using Australian acidic saline lake deposits to describe geochemical variability on Mars. Geophysical Research Letters, 36(19).

Beegle, L., Bhartia, R., White, M., DeFlores, L., Abbey, W., Wu, Y.-H., Cameron, B., Moore, J., Fries, M., Burton, A., Edgett, K.S., Ravine, M.A., Hug, W., Reid, R., Nelson, T., Clegg, S., Wiens, R., Asher, S., Sobron, P., and Ieee. (2015) SHERLOC: Scanning Habitable Environments with Raman & Luminescence for Organics & Chemicals. 2015 Ieee Aerospace Conference.

Berg, J.S., Michellod, D., Pjevac, P., Martinez-Perez, C., Buckner, C.R.T., Hach, P.F., Schubert, C.J., Milucka, J., and Kuypers, M.M.M. (2016) Intensive cryptic microbial iron cycling in the low iron water column of the meromictic Lake Cadagno. Environmental Microbiology, 18(12), 5288-5302.

Beyssac, O., Goffe, B., Petitet, J.P., Froigneux, E., Moreau, M., and Rouzaud, J.N. (2003) On the characterization of disordered and heterogeneous carbonaceous materials by Raman spectroscopy. Spectrochimica Acta Part a-Molecular and Biomolecular Spectroscopy, 59(10), 2267-2276.

Bigham, J.M., and Nordstrom, D.K. (2000) Iron and aluminum hydroxysulfates from acid sulfate waters. Sulfate Minerals - Crystallography, Geochemistry and Environmental Significance, 40, 351-403.

Bish, D.L. (1993) RIETVELD refinement of the kaolinite structure at 1.5-K. Clays and Clay Minerals, 41(6), 738-744.

Bishop, J.L. (2019) Visible and near-infrared reflectance spectroscopy of geologic materials. In J.L. Bishop, J.F. Bell III, and J.E. Moersch, Eds. Remote Compositional Analysis: Techniques for Understanding Spectroscopy, Mineralogy, and Geochemistry of Planetary Surfaces, p. 68-101. Cambridge University Press, Cambridge, UK.

Bishop, J.L., Banin, A., Mancinelli, R.L., and Klovstad, M.R. (2002) Detection of soluble and fixed NH4+ in clay minerals by DTA and IR reflectance spectroscopy: a potential tool for planetary surface exploration. Planetary and Space Science, 50(1), 11-19.

Bishop, J.L., Lane, M.D., Dyar, M.D., and Brown, A.J. (2008) Reflectance and emission spectroscopy study of four groups of phyllosilicates: smectites, kaolinite-serpentines, chlorites and micas. Clay Minerals, 43(1), 35-54.

Bishop, J.L., and Murad, E. (2005) The visible and infrared spectral properties of jarosite and

alunite. American Mineralogist, 90(7), 1100-1107.

Bishop, J.L., Parente, M., Weitz, C.M., Dobrea, E.Z.N., Roach, L.H., Murchie, S.L., McGuire, P.C., McKeown, N.K., Rossi, C.M., Brown, A.J., Calvin, W.M., Milliken, R., and Mustard, J.F. (2009) Mineralogy of Juventae Chasma: Sulfates in the light-toned mounds, mafic minerals in the bedrock, and hydrated silica and hydroxylated ferric sulfate on the plateau. Journal of Geophysical Research-Planets, 114.

Bishop, J.L., Pieters, C.M., and Edwards, J.O. (1994) Infrared spectroscopy analyses on the nature of water in montmorillonite. Clays and Clay Minerals, 42(6), 702-716.

Bishop, J.L., Schiffman, P., Murad, E., Dyar, D., M., Drief, A., and Lane, M.D. (2007) Characterization of alteration products in tephra from Haleakala, Maui: A visible-infrared spectroscopy, Mössbauer spectroscopy, XRD, EPMA and TEM study. Clays and Clay Minerals, 55, 1-17.

Bishop, J.L., Wray, J.J., Sessa, A., Danielsen, J., Ehlmann, B.L., Murchie, S.L., Horgan, B.G., Christian Parente, M., and Seelos, F.P. (2018) Evidence of salty residues in layered outcrops at Mawrth Vallis and implications for evaporative environments on early Mars. Lunar and Planetary Science Conference XLIX, p. Abstract #1117. Lunar and Planetary Institute, The Woodlands, TX.

Bladh, K.W. (1982) The formation of goethite, jarosite, and alunite during the weathering of sulfide-bearing felsic rocks. Economic Geology, 77(1), 176-184.

Bohrmann, G., Stein, R., and Faugeres, J.C. (1989) Authigenic zeolites and their relation to silica diagenesis in odp site-661 sediments (Leg-108, Eastern Equatorial Atlantic). Geologische Rundschau, 78(3), 779-792.

Bramble, M.S., Mustard, J.F., and Salvatore, M.R. (2017) The geological history of Northeast Syrtis Major, Mars. Icarus, 293, 66-93.

Brinckerhoff, W.B., Grubisic, A., Getty, S.A., Danell, R.M., Arevalo, R.D., Li, X., van Amerom, F., Castillo, M., Eigenbrode, J., Chu, P., Zacny, K., Spring, J., Casey, M., Lalime, E., and Hoehler, T. (2018) EMILI: Europan Molecular Indicators of Life Investigation. Earth and Space 2018, p. 524-532.

Bristow, T.F., Rampe, E.B., Achilles, C.N., Blake, D.F., Chipera, S.J., Craig, P., Crisp, J.A., Des Marais, D.J., Downs, R.T., Gellert, R., Grotzinger, J.P., Gupta, S., Hazen, R.M., Horgan, B., Hogancamp, J.V., Mangold, N., Mahaffy, P.R., McAdam, A.C., Ming, D.W., Morookian, J.M., Morris, R.V., Morrison, S.M., Treimans, A.H., Vanimanm, D.T., Vasavada, A.R., and Yen, A.S. (2018) Clay mineral diversity and abundance in sedimentary rocks of Gale crater, Mars. Science Advances, 4(6).

Burns, R.G. (1987) Ferric sulfates on Mars. Journal of Geophysical Research-Solid Earth and Planets, 92(B4), E570-E574.

Cady, S.L.S., John R.Gulick, Virginia G.Berger, Jeff A.Hinman, Nancy W. (2018) Siliceous hot spring deposits: Why they remain key astrobiologial targets. In N. Cabrol, and E. Grin, Eds. From Habitability to Life on Mars, p. 179-210. Elsevier, Cabrol, Nathalie Grin, Edmond.

Carter, J., Poulet, F., Bibring, J.P., Mangold, N., and Murchie, S. (2013) Hydrous minerals on Mars as seen by the CRISM and OMEGA imaging spectrometers: Updated global view. Journal of Geophysical Research-Planets, 118(4), 831-858.

Chemtob, S.M., Jolliff, B.L., Rossman, G.R., Eiler, J.M., and Arvidson, R.E. (2010) Silica coatings in the Ka'u Desert, Hawaii, a Mars analog terrain: A micromorphological,

spectral, chemical, and isotopic study. Journal of Geophysical Research-Planets, 115.

Chevrier, V., and Mathé, P. (2007) Mineralogy and evolution of the surface of Mars: a review. Planetary and Space Science, 55(3), 289-314.

Chipera, S.J., and Bish, D.L. (2013) Fitting full X-ray diffraction patterns for quantitative analysis: a method for readily quantifying crystalline and disordered phases.

Christiansen, R.I. (2001) The Quaternary and Pliocene Yellowstone Plateau volcanic field of Wyoming, Idaho, and Montana. 145 p. *U.S. Geological Survey*, Reston, VA.

Ciniglia, C., Yoon, H.S., Pollio, A., Pinto, G., and Bhattacharya, D. (2004) Hidden biodiversity of the extremophilic Cyanidiales red algae. Molecular Ecology, 13(7), 1827-1838.

Clark, R.N., King, T.V.V., Klejwa, M., Swayze, G.A., and Vergo, N. (1990) High spectral resolution reflectance spectroscopy of minerals. Journal of Geophysical Research-Solid Earth and Planets, 95(B8), 12653-12680.

Comisarow, M.B. (1993) Fundamental-aspects of FT-ICR and applications to chemistry. Hyperfine Interactions, 81(1-4), 171-178.

Cousin, A., Sautter, V., Fabre, C., Maurice, S., and Wiens, R.C. (2012) Textural and modal analyses of picritic basalts with ChemCam Laser-Induced Breakdown Spectroscopy. Journal of Geophysical Research-Planets, 117.

Crabbe, H., Fernandez, N., and Jones, F. (2015) Crystallization of jarosite in the presence of amino acids. Journal of Crystal Growth, 416, 28-33.

D'Angeli, I.M., Carbone, C., Nagostinis, M., Parise, M., Vattano, M., Madonia, G., and De Waele, J. (2018) New insights on secondary minerals from Italian sulfuric acid caves. International Journal of Speleology, 47(3), 271-291.

Dienes, T., Pastor, S.J., Schurch, S., Scott, J.R., Yao, J., Cui, S.L., and Wilkins, C.L. (1996) Fourier transform mass spectrometry - Advancing years (1992 mid 1996). Mass Spectrometry Reviews, 15(3), 163-211.

Du, Q., Liu, S.J., Cao, Z.H., and Wang, Y.Q. (2005) Ammonia removal from aqueous solution using natural Chinese clinoptilolite. Separation and Purification Technology, 44(3), 229-234.

Ehlmann, B.L., and Edwards, C.S. (2014) Mineralogy of the Martian surface. Annual Review of Earth and Planetary Sciences, Vol 42, 42, 291-315.

Ehlmann, B.L., and Mustard, J.F. (2012) An in-situ record of major environmental transitions on early Mars at Northeast Syrtis Major. Geophysical Research Letters, 39.

Ehlmann, B.L., Mustard, J.F., Murchie, S.L., Poulet, F., Bishop, J.L., Brown, A.J., Calvin, W.M., Clark, R.N., Des Marais, D.J., Milliken, R.E., Roach, L.H., Roush, T.L., Swayze, G.A., and Wray, J.J. (2008) Orbital identification of carbonate-bearing rocks on Mars. Science, 322(5909), 1828-1832.

Ehlmann, B.L., Swayze, G.A., Milliken, R.E., Mustard, J.F., Clarks, R.N., Murchie, S.L., Breit, G.N., Wray, J.J., Gondet, B., Poulet, F., Carter, J., Calvin, W.M., Benzel, W.M., and Seelos, K.D. (2016) Discovery of alunite in Cross crater, Terra Sirenum, Mars: Evidence for acidic, sulfurous waters. American Mineralogist, 101(7-8), 1527-1542.

Ellis, A.J., and Mahon, W.A.J. (1977) Chemistry and geothermal systems. 392 p. Academic Press, Cambridge, MA.

Fairen, A.G., Davila, A.F., Lim, D., Bramall, N., Bonaccorsi, R., Zavaleta, J., Uceda, E.R., Stoker, C., Wierzchos, J., Dohm, J.M., Amils, R., Andersen, D., and McKay, C.P. (2010) Astrobiology through the sges of Mars: The dtudy of terrestrial analogues to understand

the habitability of Mars. Astrobiology, 10(8), 821-843.

Farrand, W.H., Glotch, T.D., Rice, J.W., Hurowitz, J.A., and Swayze, G.A. (2009) Discovery of jarosite within the Mawrth Vallis region of Mars: Implications for the geologic history of the region. Icarus, 204(2), 478-488.

Feeley, T.C., Cosca, M.A., and Lindsay, C.R. (2002) Petrogenesis and implications of calc-alkaline cryptic hybrid magmas from Washburn volcano, Absaroka Volcanic Province, USA. Journal of Petrology, 43(4), 663-703.

Fishbain, S., Dillon, J.G., Gough, H.L., and Stahl, D.A. (2003) Linkage of high rates of sulfate reduction in Yellowstone hot springs to unique sequence types in the dissimilatory sulfate respiration pathway. Applied and Environmental Microbiology, 69(6), 3663-3667.

Fournier, R.O. (1989) Geochemistry and dynamics of the Yellowstone-National-Park hydrothermal system. Annual Review of Earth and Planetary Sciences, 17, 13-53.

Frost, R.L., Wills, R.A., Weier, M.L., Martens, W., and Mills, S. (2006) A Raman spectroscopic study of selected natural jarosites. Spectrochimica Acta Part a-Molecular and Biomolecular Spectroscopy, 63(1), 1-8.

Glamoclija, M., Garrel, L., Berthon, J., and Lopez-Garcia, P. (2004) Biosignatures and bacterial diversity in hydrothermal deposits of Solfatara Crater, Italy. Geomicrobiology Journal, 21(8), 529-541.

Glavin, D.P., Cleaves, H.J., Buch, A., Schubert, M., Aubrey, A., Bada, J.L., and Mahaffy, P.R. (2006a) Sublimation extraction coupled with gas chromatography-mass spectrometry: A new technique for future in situ analyses of purines and pyrimidines on Mars. Planetary and Space Science, 54(15), 1584-1591.

Glavin, D.P., Dworkin, J.P., Aubrey, A., Botta, O., Doty, J.H., Martins, Z., and Bada, J.L. (2006b) Amino acid analyses of Antarctic CM2 meteorites using liquid chromatography-time of flight-mass spectrometry. Meteoritics & Planetary Science, 41(6), 889-902.

Goetz, W., Brinckerhoff, W.B., Arevalo, R., Freissinet, C., Getty, S., Glavin, D.P., Siljestrom, S., Buch, A., Stalport, F., Grubisic, A., Li, X., Pinnick, V., Danell, R., van Amerom, F.H.W., Goesmann, F., Steininger, H., Grand, N., Raulin, F., Szopa, C., Meierhenrich, U., Brucato, J.R., and Team, M.S. (2016) MOMA: the challenge to search for organics and biosignatures on Mars. International Journal of Astrobiology, 15(3), 239-250.

Golden, D.C., Ming, D.W., Morris, R.V., and Mertzman, S.A. (2005) Laboratory-simulated acid-sulfate weathering of basaltic materials: Implications for formation of sulfates at Meridiani Planum and Gusev crater, Mars. Journal of Geophysical Research-Planets, 110(E12).

Gordon, P.R., and Sephton, M.A. (2016) Organic matter detection on Mars by pyrolysis-FTIR: An analysis of sensitivity and mineral matrix effects. Astrobiology, 16(11), 831-845.

Goudge, T.A., Mustard, J.F., Head, J.W., Fassett, C.I., and Wiseman, S.M. (2015a) Assessing the mineralogy of the watershed and fan deposits of the Jezero crater paleolake system, Mars. Journal of Geophysical Research-Planets, 120(4), 775-808.

Goudge, T.A., Mustard, J.F., Head, J.W., Salvatore, M.R., and Wiseman, S.M. (2015b) Integrating CRISM and TES hyperspectral data to characterize a halloysite-bearing deposit in Kashira crater, Mars. Icarus, 250, 165-187.

Groenewold, G.S., Hodges, B.D., Scott, J.R., Gianotto, A.K., Appelhans, A.D., Kessinger, G.F., and Wright, J. (2001) Oxygen-for-sulfur exchange in the gas phase: Reactions of Al and Si oxyanions with H2S. The Journal of Physical Chemistry A, 105(16), 4059-4064.

Hays, L.E., Graham, H.V., Marais, D.J.D., Hausrath, E.M., Horgan, B., McCollom, T.M., Parenteau, M.N., Potter-McIntyre, S.L., Williams, A.J., and Lynch, K.L. (2017) Biosignature preservation and detection in Mars analog environments. Astrobiology, 17(4), 363-+.

Heeren, R.M.A., Kleinnijenhuis, A.J., McDonnell, L.A., and Mize, T.H. (2004) A mini-review of mass spectrometry using high-performance FTICR-MS methods. Analytical and Bioanalytical Chemistry, 378(4), 1048-1058.

Henneberger, R.M. (2008) The microbial diversity and ecology of selected andesitic hydrothermal environments. Macquarie University, Australia.

Ji, Z.-Y., Yuan, J.-S., and Li, X.-G. (2007) Removal of ammonium from wastewater using calcium form clinoptilolite. Journal of Hazardous Materials, 141(3), 483-488.

Jones, B., and Renaut, R.W. (2007) Selective mineralization of microbes in Fe-rich precipitates (jarosite, hydrous ferric oxides) from acid hot springs in the Waiotapu geothermal area, North Island, New Zealand. Sedimentary Geology, 194(1-2), 77-98.

Kaksonen, A.H., Morris, C., Wylie, J., Li, J., Usher, K., Hilario, F., and du Plessis, C.A. (2017) Continuous flow 70° C archaeal bioreactor for iron oxidation and jarosite precipitation. Hydrometallurgy, 168, 40-48.

Khoshkhoo, M., Dopson, M., and Sandström, Å. (2015) Role of microbial activity in bioleaching of a pyritic and a pure chalcopyrite concentrate. Advanced Materials Research, 1130, p. 209-213. Trans Tech Publ.

Klingelhofer, G. (2004) Mossbauer in situ studies of the surface of Mars. Hyperfine Interactions, 158(1-4), 117-124.

Kosek, F., Culka, A., and Jehlicka, J. (2018) Raman spectroscopic study of six synthetic anhydrous sulfates relevant to the mineralogy of fumaroles. Journal of Raman Spectroscopy, 49(7), 1205-1216.

Kotler, J.M., Hinman, N.W., Richardson, C.D., and Scott, J.R. (2010) Thermal decomposition behavior of potassium and sodium jarosite synthesized in the presence of methylamine and alanine. Journal of Thermal Analysis and Calorimetry, 102(1), 23-29.

Kotler, J.M., Hinman, N.W., Yan, B., Stoner, D.L., and Scott, J.R. (2008) Glycine identification in natural jarosites using laser desorption Fourier transform mass spectrometry: Implications for the search for life on Mars. Astrobiology, 8(2), 253-266.

Kruszewski, L. (2013) Supergene sulphate minerals from the burning coal mining dumps in the Upper Silesian Coal Basin, South Poland. International Journal of Coal Geology, 105, 91-109.

Lane, M.D., and Bishop, J.L. (2019) Mid-infrared (thermal) emission and reflectance spectroscopy. Remote Compositional Analysis: Techniques for Understanding Spectroscopy, Mineralogy, and Geochemistry of Planetary Surfaces, p. 42-67. Cambridge University Press, Cambridge, UK.

Lanzarotta, A. (2015) Approximating the detection limit of an infrared spectroscopic imaging microscope operating in an attenuated total reflection (ATR) modality: Theoretical and empirical results for an instrument using a linear array detector and a 1.5 millimeter germanium hemisphere internal reflection element. Applied Spectroscopy, 69(2), 205-214.

Leman, J. (2009) Lipids, Production. Encyclopedia of Microbiology, 3e, p. 396-397. Academic Press.

Lewis, J.M.T., Watson, J.S., Najorka, J., Duy, L., and Sephton, M.A. (2015) Sulfate minerals: A problem for the detection of organic compounds on Mars? Astrobiology, 15(3), 247-258.

Ling, Z., Cao, F., Ni, Y., Wu, Z., Zhang, J., and Li, B. (2016) Correlated analysis of chemical variations with spectroscopic features of the K–Na jarosite solid solutions relevant to Mars. Icarus, 271, 19-29.

Madden, M.E.E., Bodnar, R.J., and Rimstidt, J.D. (2004) Jarosite as an indicator of water-limited chemical weathering on Mars. Nature, 431(7010), 821-823.

Marshall, A.G.V., F.R. (1990) r
Transforms in NMR, Optical, and Mass Spectrometry: A User's Handbook. Elsevier, New York.

Martins, Z., Cottin, H., Kotler, J.M., Carrasco, N., Cockell, C.S., de la Torre Noetzel, R., Demets, R., De Vera, J.-P., d'Hendecourt, L., and Ehrenfreund, P. (2017) Earth as a Tool for Astrobiology—A European Perspective. Space Science Reviews, 209(1-4), 43-81.

McHenry, L.J., Carson, G.L., Dixon, D.T., and Vickery, C.L. (2017) Secondary minerals associated with Lassen fumaroles and hot springs: Implications for martian hydrothermal deposits. American Mineralogist, 102(7), 1418-1434.

McJunkin, T.R., and Scott, J.R. (2010) Application of Fuzzy logic for automated interpretation of mass spectra. In R.E. Vargas, Ed. Fuzzy Logic: Theory, Programming and Applications, p. 85–114. Nova Science Publishers, Hauppauge, NY.

McJunkin, T.R., Tremblay, P.L., and Scott, J.R. (2002) Automation and control of an imaging internal laser desorption Fourier transform mass spectrometer (I2LD-FTMS). JALA: Journal of the Association for Laboratory Automation, 7(3), 76-83.

Meerdink, S.K., Hook, S.J., Roberts, D.A., and Abbott, E.A. (2019) The ECOSTRESS spectral library version 1.0. Remote Sensing of Environment, 230.

Ming, D.W. (2019) Aqueous alteration on Mars. 2018-2019 International Soils Meeting. Soil Science Society of America, San Diego, CA USA.

Morris, R.V., Klingelhofer, G., Schroder, C., Rodionov, D.S., Yen, A., Ming, D.W., de Souza, P.A., Wdowiak, T., Fleischer, I., Gellert, R., Bernhardt, B., Bonnes, U., Cohen, B.A., Evlanov, E.N., Foh, J., Gutlich, P., Kankeleit, E., McCoy, T., Mittlefehldt, D.W., Renz, F., Schmidt, M.E., Zubkov, B., Squyres, S.W., and Arvidson, R.E. (2006) Mossbauer mineralogy of rock, soil, and dust at Meridiani Planum, Mars: Opportunity's journey across sulfate-rich outcrop, basaltic sand and dust, and hematite lag deposits. Journal of Geophysical Research-Planets, 111(E12).

Murchie, S.L., Mustard, J.F., Ehlmann, B.L., Milliken, R.E., Bishop, J.L., McKeown, N.K., Dobrea, E.Z.N., Seelos, F.P., Buczkowski, D.L., Wiseman, S.M., Arvidson, R.E., Wray, J.J., Swayze, G., Clark, R.N., Marais, D.J.D., McEwen, A.S., and Bibring, J.P. (2009) A synthesis of Martian aqueous mineralogy after 1 Mars year of observations from the Mars Reconnaissance Orbiter. Journal of Geophysical Research-Planets, 114.

Murphy, W.M., and Helgeson, H.C. (1987) Thermodynamic and kinetic constraints on reaction-rates among minerals and aqueous-solutions. 3. activated complexes and the pH-dependence of the rates of feldspar, pyroxene, wollastonite, and olivine hydrolysis. Geochimica Et Cosmochimica Acta, 51(12), 3137-3153.

Nachon, M., Mangold, N., Forni, O., Kah, L.C., Cousin, A., Wiens, R.C., Anderson, R., Blaney, D., Blank, J.G., and Calef, F. (2017) Chemistry of diagenetic features analyzed by ChemCam at Pahrump Hills, Gale crater, Mars. Icarus, 281, 121-136.

Nathan, Y., and Flexer, A. (1977) Clinoptilolite, paragenesis and stratigraphy. Sedimentology, 24(6), 845-855.

Nna-Mvondo, D., and Martinez-Frias, J. (2007) Review komatiites: from Earth's geological settings to planetary and astrobiological contexts. Earth Moon and Planets, 100(3-4), 157-179.

Nordstrom, D.K. (1982) Aqueous pyrite oxidation and the consequent formation of secondary iron minerals. SSSA Special Publication, 10, 37-56.

Oelkers, E.H., and Schott, J. (2001) An experimental study of enstatite dissolution rates as a function of pH, temperature, and aqueous Mg and Si concentration, and the mechanism of pyroxene/pyroxenoid dissolution. Geochimica Et Cosmochimica Acta, 65(8), 1219-1231.

Orofino, V., Blanco, A., D'Elia, M., Licchelli, D., Fonti, S., and Marzo, G.A. (2010) Study of terrestrial fossils in phyllosilicate-rich soils: Implication in the search for biosignatures on Mars. Icarus, 208(1), 202-206.

Papike, J.J., Karner, J.M., and Shearer, C.K. (2006) Comparative planetary mineralogy: Implications of martian and terrestrial jarosite. A crystal chemical perspective. Geochimica Et Cosmochimica Acta, 70(5), 1309-1321.

Pinto, G., Albertano, P., Ciniglia, C., Cozzolino, S., Pollio, A., Yoon, H.S., and Bhattacharya, D. (2003) Comparative approaches to the taxonomy of the genus Galdieria Merola (Cyanidiales, Rhodophyta). Cryptogamie Algologie, 24(1), 13-32.

Richardson, C.D., Hinman, N.W., McJunkin, T.R., Kotler, J.M., and Scott, J.R. (2008) Exploring Biosignatures Associated with Thenardite by Geomatrix-Assisted Laser Desorption/Ionization Fourier Transform Ion Cyclotron Resonance Mass Spectrometry (GALDI-FTICR-MS). Geomicrobiology Journal, 25(7-8), 432-440.

Robertson, K.M., Milliken, R.E., and Li, S. (2016) Estimating mineral abundances of clay and gypsum mixtures using radiative transfer models applied to visible-near infrared reflectance spectra. Icarus, 277, 171-186.

Rodgers, K.A., Browne, P.R.L., Buddle, T.F., Cook, K.L., Greatrex, R.A., Hampton, W.A., Herdianita, N.R., Holland, G.R., Lynne, B.Y., Martin, R., Newton, Z., Pastars, D., Sannazarro, K.L., and Treece, C.I.A. (2004) Silica phases in sinters and residues from geothermal fields of New Zealand. Earth-Science Reviews, 66(1-2), 1-61.

Rodgers, K.A., Hamlin, K.A., Browne, P.R.L., Campbell, K.A., and Martin, R. (2000) The steam condensate alteration mineralogy of Ruatapu cave, Orakei Korako geothermal field, Taupo Volcanic Zone, New Zealand. Mineralogical Magazine, 64(1), 125-142.

Rodman, A. (1996) Soils of Yellowstone National Park. (ed Service Np). Yellowstone Center for Resources, Yellowstone National Park, WY, p. 324. National Park Service, Yellowstone National Park.

Ruff, S.W., and Farmer, J.D. (2016) Silica deposits on Mars with features resembling hot spring biosignatures at El Tatio in Chile. Nature Communications, 7.

Ruff, S.W., Farmer, J.D., Calvin, W.M., Herkenhoff, K.E., Johnson, J.R., Morris, R.V., Rice, M.S., Arvidson, R.E., Bell, J.F., Christensen, P.R., and Squyres, S.W. (2011) Characteristics, distribution, origin, and significance of opaline silica observed by the Spirit rover in Gusev crater, Mars. Journal of Geophysical Research-Planets, 116.

Rye, R.O. (2005) A review of the stable-isotope geochemistry of sulfate minerals in selected igneous environments and related hydrothermal systems. Chemical Geology, 215(1-4), 5-

36.
Saper, L., and Mustard, J.F. (2013) Extensive linear ridge networks in Nili Fossae and Nilosyrtis, Mars: implications for fluid flow in the ancient crust. Geophysical Research Letters, 40(2), 245-249.
Sasaki, K., Tanaike, O., and Konno, H. (1998) Distinction of jarosite-group compounds by Raman spectroscopy. Canadian Mineralogist, 36, 1225-1235.
Schaef, H.T., Horner, J.A., Owen, A.T., Thompson, C.J., Loring, J.S., and McGrail, B.P. (2014) Mineralization of Basalts in the CO2-H2O-SO2-O-2 System. Environmental Science & Technology, 48(9), 5298-5305.
Schiffman, P., Zierenberg, R., Marks, N., Bishop, J.L., and Dyar, M.D. (2006) Acid-fog deposition at Kilauea volcano: A possible mechanism for the formation of siliceous-sulfate rock coatings on Mars. Geology, 34(11), 921-924.
Scott, J.R., and Tremblay, P.L. (2002) Highly reproducible laser beam scanning device for an internal source laser desorption microprobe Fourier transform mass spectrometer. Review of Scientific Instruments, 73(3), 1108-1116.
Scott, J.R., Yan, B., and Stoner, D.L. (2006) Spatially-correlated mass spectrometric analysis of microbe–mineral interactions. Journal of Microbiological Methods, 67(2), 381-384.
Sergeeva, A.V., Zhitova, E.S., and Bocharov, V.N. (2019) Infrared and Raman spectroscopy of tschermigite,(NH4) Al (SO4) 2·
12H2O. Vibrational Spectroscopy, 105.
Sessa, A., Wray, J., and Bishop, J. (2018) Discovery of alunite in candidate ExoMars landing site, Mawrth Vallis: Evidence for localized evaporative environments. Lunar and Planetary Science Conference, 49.
Sharma, S.K., and Egan, M.J. (2019) Raman spectroscopy. Theory and laboratory spectra of geologic materials. In J.L. Bishop, J.F. Bell, and J.E. Moersch, Eds. Remote Compositional Analysis: Techniques for Understanding Spectroscopy, Mineralogy, and Geochemistry of
Planetary Surfaces, p. 120-146. Cambridge University Press, Cambridge, UK.
Shimobayashi, N., Ohnishi, M., and Miura, H. (2011) Ammonium sulfate minerals from Mikasa, Hokkaido, Japan: boussingaultite, godovikovite, efremovite and tschermigite. Journal of Mineralogical and Petrological Sciences, 106(3), 158-163.
Singh, M., Rajesh, V.J., Sajinkumar, K.S., Sajeev, K., and Kumar, S.N. (2016) Spectral and chemical characterization of jarosite in a palaeolacustrine depositional environment in Warkalli Formation in Kerala, South India and its implications. Spectrochimica Acta Part A Molecular and Biomolecular Spectroscopy, 168, 86-97.
Skelley, A.M., Scherer, J.R., Aubrey, A.D., Grover, W.H., Ivester, R.H.C., Ehrenfreund, P., Grunthaner, F.J., Bada, J.L., and Mathies, R.A. (2005) Development and evaluation of a microdevice for amino acid biomarker detection and analysis on Mars. Proceedings of the National Academy of Sciences of the United States of America, 102(4), 1041-1046.
Sobron, P., Bishop, J.L., Blake, D.F., Chen, B., and Rull, F. (2014) Natural Fe-bearing oxides and sulfates from the Rio Tinto Mars analog site: Critical assessment of VNIR reflectance spectroscopy, laser Raman spectroscopy, and XRD as mineral identification tools. American Mineralogist, 99(7), 1199-1205.
Spear, J.R., Walker, J.J., McCollom, T.M., and Pace, N.R. (2005) Hydrogen and bioenergetics in the Yellowstone geothermal ecosystem. Proceedings of the National Academy of

Sciences of the United States of America, 102(7), 2555-2560.

Squyres, S.W., Arvidson, R.E., Ruff, S., Gellert, R., Morris, R.V., Ming, D.W., Crumpler, L., Farmer, J.D., Des Marais, D.J., Yen, A., McLennan, S.M., Calvin, W., Bell, J.F., III, Clark, B.C., Wang, A., McCoy, T.J., Schmidt, M.E., and de Souza, P.A., Jr. (2008) Detection of silica-rich deposits on Mars. Science, 320(5879), 1063-1067.

Stack, K.M., and Milliken, R.E. (2015) Modeling near-infrared reflectance spectra of clay and sulfate mixtures and implications for Mars. Icarus, 250, 332-356.

Stoffregen, R.E. (1993) Stability relations of jarosite and natrojarosite at 150-250-degrees-C. Geochimica Et Cosmochimica Acta, 57(11), 2417-2429.

Stumm, W., and Morgan, J.J. (2012) Aquatic chemistry: chemical equilibria and rates in natural waters. John Wiley & Sons.

Summons, R.E., Amend, J.P., Bish, D., Buick, R., Cody, G.D., Des Marais, D.J., Dromart, G., Eigenbrode, J.L., Knoll, A.H., and Sumner, D.Y. (2011) Preservation of Martian Organic and Environmental Records: Final Report of the Mars Biosignature Working Group. Astrobiology, 11(2), 157-181.

Susi, H., Byler, D., and Damert, W. (1980) Raman intensities of carbon-carbon stretching modes in a model membrane. Chemistry and Physics of Lipids, 27(4), 337-344.

Swayze, G., Ehlmann, B., Milliken, R., Poulet, F., Wray, J., Rye, R., Clark, R., Desborough, G., Crowley, J., and Gondet, B. (2008) Discovery of the acid-sulfate mineral alunite in Terra Sirenum, Mars, using MRO CRISM: Possible evidence for acid-saline lacustrine deposits? AGU Fall Meeting Abstracts.

Velbel, M.A. (1989) Weathering of hornblende to ferruginous products by a dissolution-reprecipitation mechanism - petrography and stoichiometry. Clays and Clay Minerals, 37(6), 515-524.

Wang, A., Freeman, J.J., and Jolliff, B.L. (2015) Understanding the Raman spectral features of phyllosilicates. Journal of Raman Spectroscopy, 46(10), 829-845.

Wopenka, B., and Pasteris, J.D. (1993) Structural characterization of kerogens to granulite-facies graphite - applicability of Raman microprobe spectroscopy. American Mineralogist, 78(5-6), 533-557.

Wray, J.J., Squyres, S.W., Roach, L.H., Bishop, J.L., Mustard, J.F., and Dobrea, E.Z.N. (2010) Identification of the Ca-sulfate bassanite in Mawrth Vallis, Mars. Icarus, 209(2), 416-421.

Yan, B., McJunkin, T.R., Stoner, D.L., and Scott, J.R. (2006) Validation of fuzzy logic method for automated mass spectral classification for mineral imaging. Applied Surface Science, 253(4), 2011-2017.

Yan, B.Z., Stoner, D.L., Kotler, J.M., Hinman, N.W., and Scott, J.R. (2007a) Detection of biosignatures by geomatrix-assisted laser desorption/ionization (GALDI) mass spectrometry. Geomicrobiology Journal, 24(3-4), 379-385.

Yan, B.Z., Stoner, D.L., and Scott, J.R. (2007b) Direct LD-FTMS detection of mineral-associated PAHs and their influence on the detection of co-existing amino acids. Talanta, 72(2), 634-641.

Ye, C., and Glotch, T.D. (2016) VNIR and MIR spectral features and detection limits of minor phases in chloride-bearing mineral mixtures. AGUFM, p. P21C-2123.

Zimbelman, D.R., Rye, R.O., and Breit, G.N. (2005) Origin of secondary sulfate minerals on active andesitic stratovolcanoes. Chemical Geology, 215(1-4), 37-60.

Tables.

Table 1. Sampling site properties and analysis matrix.

Sample / site ID	***Sample type***	***Coordinates (elevation)***	***Surface Temp. (^{O}C)***	***Temp. (^{O}C) depth (cm)***	***pH (±0.1)***	***Soil chemistry***	***Mineralogy (XRD, VNIR, Raman)***	***LD-FTMS***	***Water chemistry***
W1	*soil*	N44^{O}46'00.8", W110^{O}25'47.4" (2532 m)	62 - 75	91°C (10)	1.6 - 1.9	+	+	+	
W2	*boulder*	N44^{O}46'00.0", W110^{O}25'40.1" (2535 m)	36 - 47	68°C (1), 89.9^{O}C (5)	1.1 - 2.7	+	+	+	
W4	*soil*	N44^{O}45'53.6", W110^{O}25'45.8" (2507 m)	ND	71.7^{O}C (2), 85.2^{O}C (5)	1.7 - 2.2	+	+		
WS5 / WWS5	*soil/water*	N44^{O}45'53.18", W110^{O}25'48.23" (2477 m)	77.5		3.6±*0.1*		+		+
WS8 / WWS8	*soil/water*	N 44 45' 59.85", W110 25'48.81" (2526 m)	43.7		4.6±*0.1*		+		+
W3	*background soil*	N44^{O}45'55.2", W110^{O}25'48.1" (2508 m)	24.4 - 29	29°C (1)	3.4 - 3.6	+	+		
Blank	*water*	Milli-Q water							+
+ = analysis completed									

Table 2. Temperature and major element bulk concentrations* for Al-bearing silicate site (W1), jarosite site (W2), and the 'background' site (W3). Analyses were performed by XRF at a commercial laboratory (SGS, Lakeview, Ontario, Canada).

Component*	W1**	W2	W4	Background (W3)
Temperature (°C) and	62-75	36-47	71-85	29
pH of slurry	1.6-1.9	1.1-2.7	1.7-2.2	3.4-3.6
Surface water present	no	no	no	no
[C] wt%	1.28	0.69	1.19	14.10
[S] wt%	0.73	1.85	1.05	0.31
SiO_2 wt%	85.50	87.00	82.2	55.20
Al_2O_3 wt%	0.52	0.81	0.39	9.06
Fe_2O_3 wt%	0.57	0.32	0.95	2.00
TiO_2 wt%	3.49	1.8	7.72	0.38
K_2O wt%	0.06	0.09	0.06	2.99
CaO wt%	0.03	0.06	0.02	0.37
Na_2O wt%	0.08	0.10	0.10	0.63
MgO wt%	0.22	0.21	0.30	0.43

*Error was 10 wt% of the reported value. For example, [C] = 1.28 ± 0.13 wt%.
** = Analysis duplicated, average reported.

Table 3. Minerals and organic matter detected in subsamples from WHS. Quantitative analysis by Rietveld refinement shown in shaded cells.

Component	W1	W2	WS8*	WS5*
	n=2	n=2	n=3	n=3
Alunite		41.6	19.6	
Ammoniojarosite			yes	
Hydroniumjarosite			40.2	
Jarosite		15.5	22.6	
Anatase	< 10			
Carlsonite			17.6	
Clairite			yes	
Copiapite				yes
Lonecreekite				
Mohrite				33
Sabieite				7.5
Tschermigite			yes	45
Clinoptilolite			yes	13.3
Kaolinite			yes	
Quartz	> 90	42.5	yes	1.1
Amorphous	no	yes	yes	yes
Combined LD-FTMS and Raman spectroscopy analyses – Summary results for detection of organic matter.				
Organic matter presence and diversity **	x	xx	nd	nd

* Less than 1 g of sample was collected for detailed mineralogical, spectroscopic, and spectrometric analyses. **Combines information on the presence and diversity (as m/z for LD-FTMS and as number of organic bond types for Raman microscopy. 'nd' is not detected. 'x' is present. 'xx' is greater diversity and more frequent detections (presence). W4 data are not shown.

Table 4. GALDI-FTMS peaks detected in W1 and W2 from WHS. The assigned ion composition is based on analysis of the m/z* and the mass defect. Organic species are identified in bold type.

Peak(s)	Presence in sample	Assigned ion	Comments
38.963, 40.961	W1	K^+	K isotopes
39.962	W1	Ca^+	
53.939, 55.934	W1	Fe^+	Fe isotopes
38.963, 40.96, 53.939, 55.934	W2	K^+, Fe^+	Found together in jarosite
45.952	W1	Ti^+	
61.947	W1	TiO^+	
137.905	W1	Ba^+	
154.908	W1	$BaOH^+$	
201.221	W2	$\mathbf{C_{13}H_{31}N^+}$	
315.253	W2	$\mathbf{C_{16}H_{38}NO_2K^+}$	
318.869	W2		Unassigned, inorganic
319.107	W2	$\mathbf{C_{14}H_{25}O_3K_2^+}$	
371.139	W2	$\mathbf{C_{18}H_{29}O_3K_2^+}$	
428.787	W1	$Al_5Si_3O_{13}H_2^+$	Al-bearing silicate
438.491	W2	$\mathbf{C_{29}H_{62}N_2^+}$	
448.839	W1	$Al_7SiO_{14}H_8$+	Al-bearing silicate
472.708	W1	$Al_5Si_3O_4S_4H_6^+$	Possible alunite
2035	W1	**Organic**	Not resolved
3900	W1	**Organic**	Not resolved
4150	W1	**Organic**	Not resolved
6600	W2	**Organic**	Not resolved

*Error is ±0.003 amu except for peaks >2000, which are not sufficiently resolved to make compositional assignments.

8 Figure Captions

Figure 1: Location of study site. (a) Location of Yellowstone National Park, WY, in western U.S.A., (b) Location of WHS in Yellowstone National Park, WY, (c) Location of soil-sample sites (orange), disintegrating boulder site (red), and water sample sites (blue) in WHS.

Figure 2. Photographs of WHS showing the disintegrating boulder (W2). (a) Overview of site showing distinct areas of yellow materials, gray/buff materials, and small textured mounds of disintegrating boulders. (b) Close-up of undisturbed disintegrating boulder (W2). (c) Close-up of excavated profile of W2. Spatula is 17.6 cm.

Figure 3. GALDI-FTMS spectra of W1 sample illustrating heterogeneous distribution of species. The figure shows a 1.5 mm x 1.5 mm map of the sample surface. Each dot represents a single laser shot and therefore a spectrum. The legend shows the interpreted elemental composition derived from the spectra or the m/z of unassigned but distinctive peaks. The surrounding insets illustrate the spectra associated with each type of material in the sample. The pseudo-image or map of the sample provides a visual representation of the relative chemical compositions across the surface of the sample. (a) Map of spectra collected from a powdered sample. (b) Other common inorganic signatures included Ti, TiO, Ba, and BaOH at m/z 45.952, 61.947, 137.905, and 154.907, respectively. (c) Ca-dominated background, (d) Al-bearing silicate species at m/z 428.787 and 448.839, (E) Al-bearing silicate species at m/z 472.708 with sulfur incorporated, and (F) higher mass species with m/z values > 2000.

Figure 4. GALDI-FTMS spectra of W2 sample illustrating heterogeneous distribution of species. Refer to Figure 3 for explanation of central map. (a) Map of spectra collected from a powdered sample. (b) Spectra shown for (a) m/z 319.107 and 371.139 species with mass defects indicative of organic species and (c) peaks around m/z 6600. See Fig. 3 for examples of spectra >2000 u and for background inorganic species.

Figure 5. Raman spectra of WHS samples. (a) Eleven spectra from three sites are shown along with the standards for quartz, tschermigite, jarosite, alunite, and copiapite. Nine spectra from WS8 were collected on subsamples with different visual properties (texture, grain size, color) demonstrating the heterogeneous nature of the samples. Quartz, jarosite, and alunite were identified in several samples. Tschermigite was identified in one sample, but copiapite was not observed by Raman spectroscopy, although both were observed by XRD. (b) WS8-yellow-1 exhibited organic fluorescence and Raman bands in the 1200-1800 cm^{-1} region with 1219 and 1311 cm^{-1} corresponding to ring vibrations or CH_2 and in-plane CH deformation, respectively. The band at 1605 cm^{-1} could be assigned to NH_2. WS8-buff exhibited jarosite peaks at 1009 cm^{-1}, 1103 cm^{-1} (CC stretching mode), and 1147/1154 cm^{-1}; alunite peaks at 1027/1036 cm^{-1} (CC stretching modes); and a tschermigite peak at 994 cm^{-1}. C=C stretching modes occur near 1000-1200 cm-1 (e.g., Susi et al 1980) and

contribute to the features observed in this region adding complexity to the bands due to sulfate vibrations.

Figure 6. X-ray diffraction patterns from site W2. (a) SEM image (scale bar is 5 μm). EDS chemistry could not be obtained due to sample charging. (b) XRD pattern. Jrs = jarosite, Qz = quartz, Alu = alunite, Si = internal Si standard (4 wt%). After correction for the internal standard, the sample is 6.7 wt% quartz, 6.5 wt% alunite, 2.4 wt% jarosite, and over 80 wt% amorphous material, which could have crystal size below the resolution by XRD.

Figure 7. Washburn sample WS8. (a) SEM image (scale bar equals 10 μm). (b) EDS chemistry of (a) with oxygen, iron, aluminum, silicon, sulfur and potassium. (c) XRD diffractogram (Cpt – Na-clinoptilolite, Jrs - jarosite, Alu - alunite, Qz – quartz).

Figure 8. Washburn sample WS5. (a) SEM image of jarosite crystals with (b) corresponding EDS spectra showing O, Fe, Na, Mg, Al, Si, and S (scale bar = 10 μm). (c) SEM image of unknown mineral with (d) corresponding EDS chemistry with O, Mg, and S (scale bar = 5 μm). (e) XRD diffractogram with copiapite (Cop), kaolinite (Kln), clinoptilolite-Na (Cpt), tschermigite (Tsh), and quartz (Qz).

Figure 9. VNIR reflectance spectra of WHS samples compared with minerals. (a) spectra for gray/buff samples from 0.35 to 2.5 μm showing several features due to H_2O, OH, NH_4, and sulfate in these samples, (b) spectra from 1.3-2.5 μm including also NH_4-bearing minerals. Vertical lines mark features due to minerals or species in these samples: dotted lines at 1.41 and 1.91 μm due to bound H_2O in clays (Bishop et al., 1994) or zeolite (e.g., clinoptilolite, USGS spectral library, Clark et al., 1990), dashed lines at 1.45-1.48 and 1.94-1.97 μm due to H_2O in hydrated sulfates such as hexahydrite (e.g., Bishop et al., 2009) or tschermigite (speclib.jpl.nasa.gov/library; Meerdink et al., 2019), solid lines at 1.56, 2.01 and 2.11 μm due to NH_4^+ in minerals (e.g., Bishop et al., 2002; Berg et al., 2016), yellow solid lines at 1.47 and 2.26 μm due to Fe-OH in jarosite (Bishop and Murad, 2005), broken lines at 2.17 and 2.21 μm due to Al-OH in alunite (Bishop and Murad, 2005) and montmorillonite (e.g., Bishop et al., 2008), respectively.

Fig 1

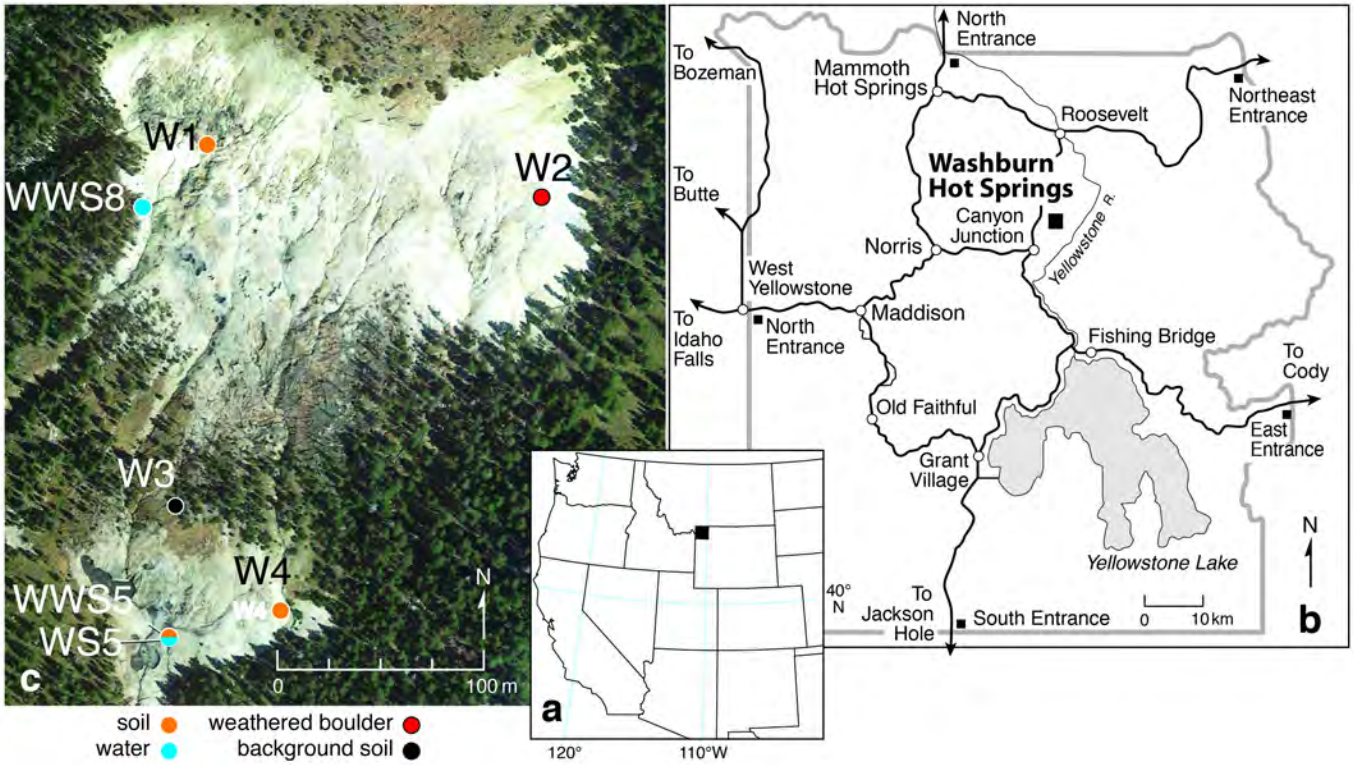
W1
W2
WWS8
W3
W4
WWS5
WS5
c
N
0
100 m
soil
water
weathered boulder
background soil
a
40° N
120°
110°W
North Entrance
To Bozeman
Mammoth Hot Springs
Northeast Entrance
Roosevelt
Washburn Hot Springs
To Butte
Canyon Junction
Yellowstone R.
Norris
West Yellowstone
Maddison
To Idaho Falls
North Entrance
Fishing Bridge
To Cody
Old Faithful
East Entrance
Grant Village
Yellowstone Lake
N
To Jackson Hole
South Entrance
0
10 km
b

Fig 2

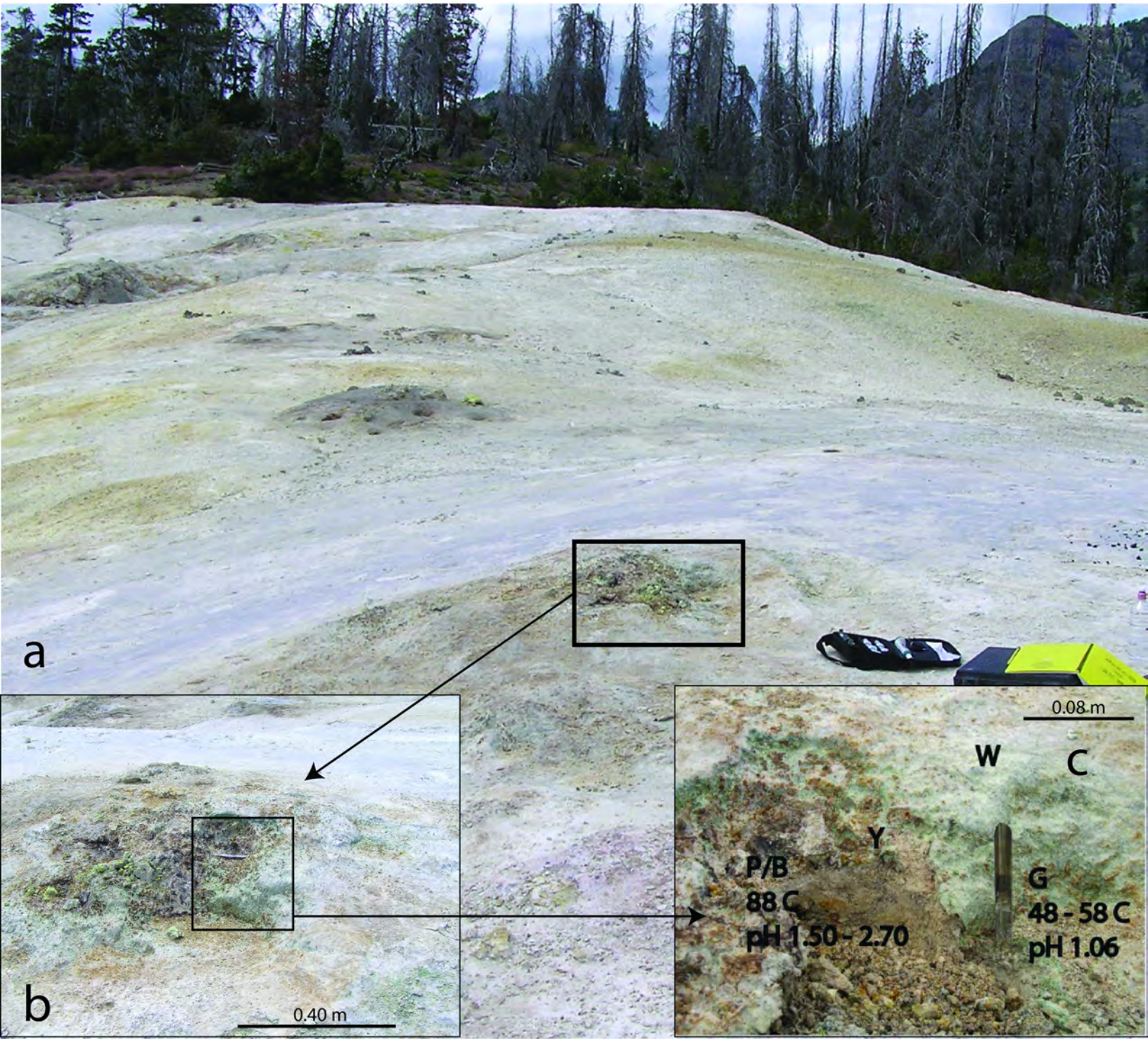

Fig 3

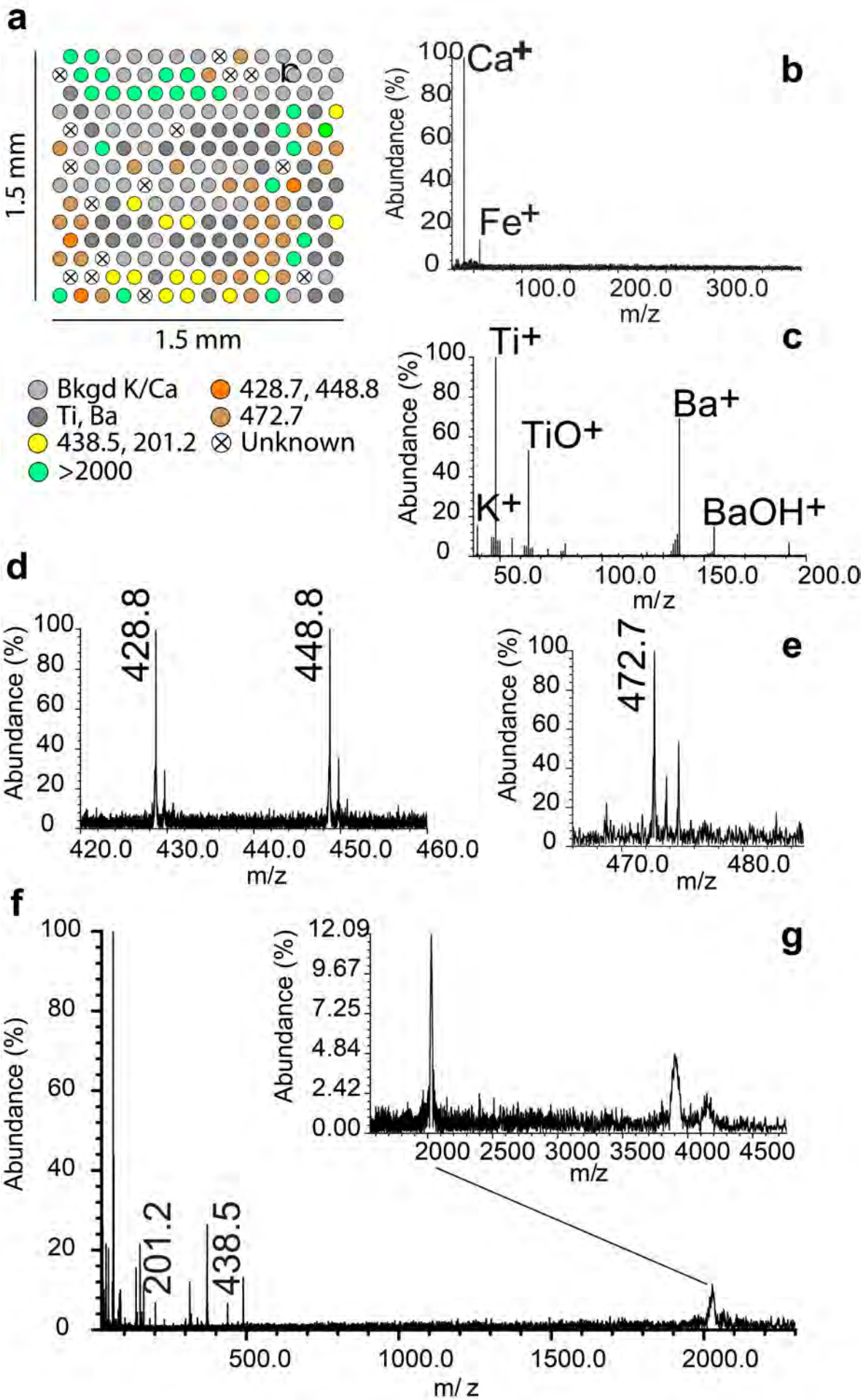
a
1.5 mm
1.5 mm
Bkgd K/Ca
Ti, Ba
438.5, 201.2
>2000
428.7, 448.8
472.7
Unknown
b
Ca+
Fe+
Abundance (%)
m/z
c
Ti+
TiO+
K+
Ba+
BaOH+
Abundance (%)
m/z
d
428.8
448.8
Abundance (%)
m/z
e
472.7
Abundance (%)
m/z
f
201.2
438.5
Abundance (%)
m/z
g
Abundance (%)
m/z

Fig 4

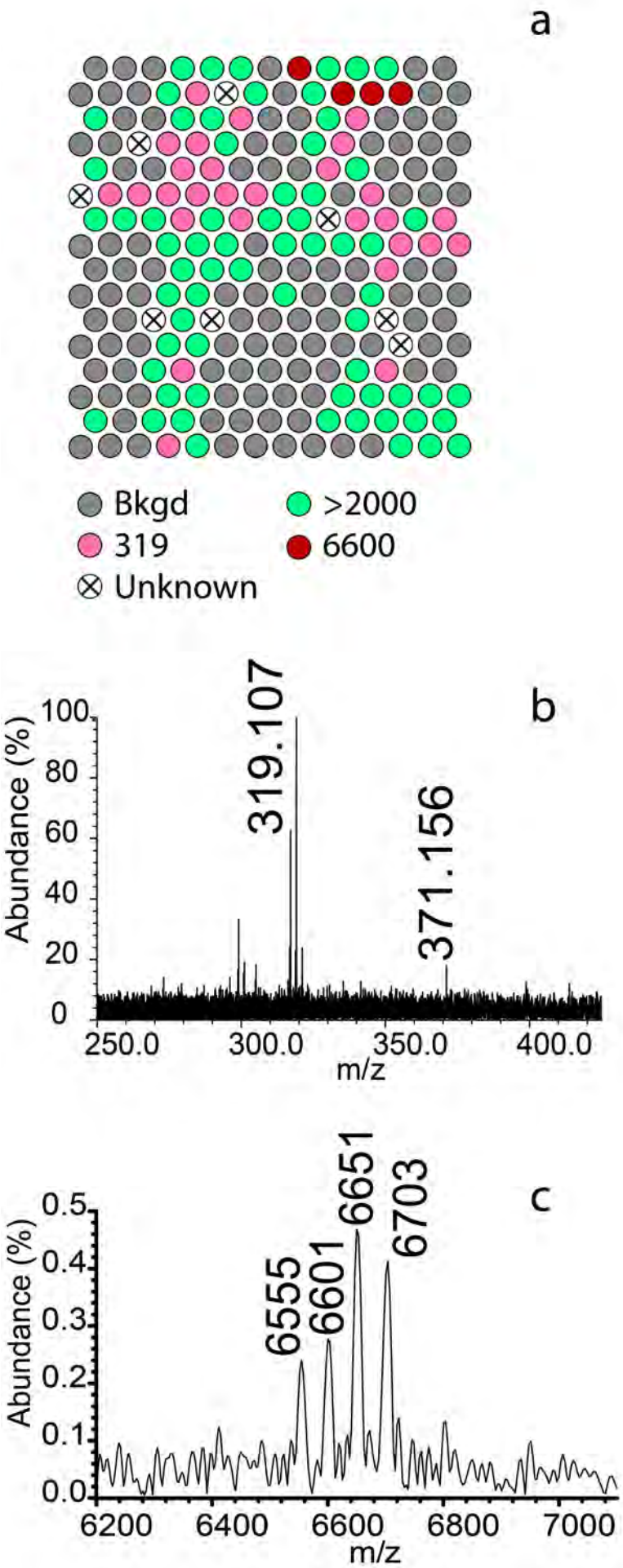
a
Bkgd
>2000
319
6600
Unknown
b
319.107
371.156
Abundance (%)
100
80
60
40
20
0
250.0
300.0
350.0
400.0
m/z
c
6555
6601
6651
6703
Abundance (%)
0.5
0.4
0.3
0.2
0.1
0.0
6200
6400
6600
6800
7000
m/z

Fig 5a

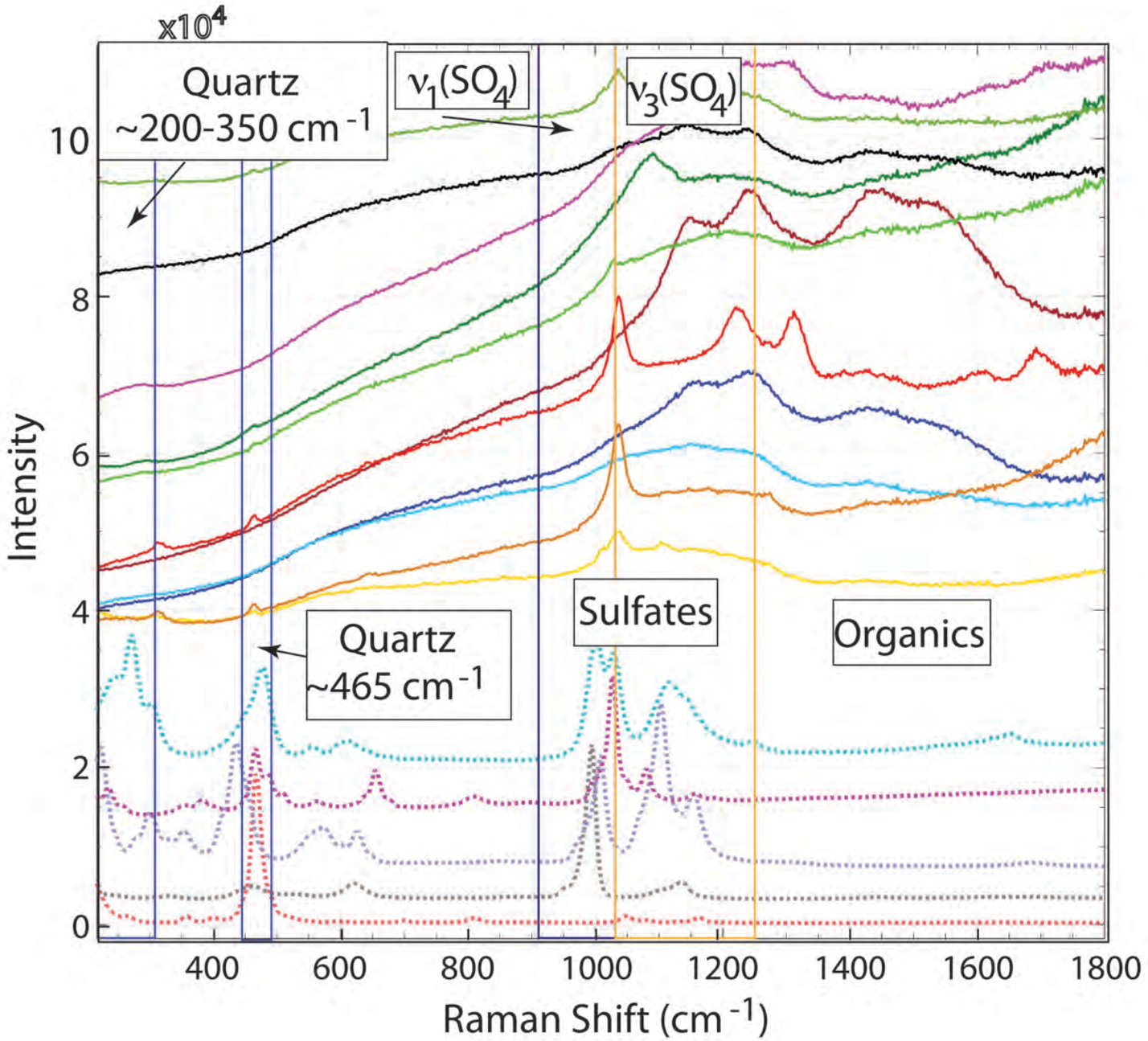

WS8-yellow-1
WS8-yellow-1
WS8-gray
WS8-gray
WS8-yellow chunks
WS8-yellow chunks
WS8-buff
WS8-buff

WS8-yellow-2
WS2-brown
WS5-cherty
Quartz
Tschermigite
Jarosite
Alunite
Copiapite

Fig 5b

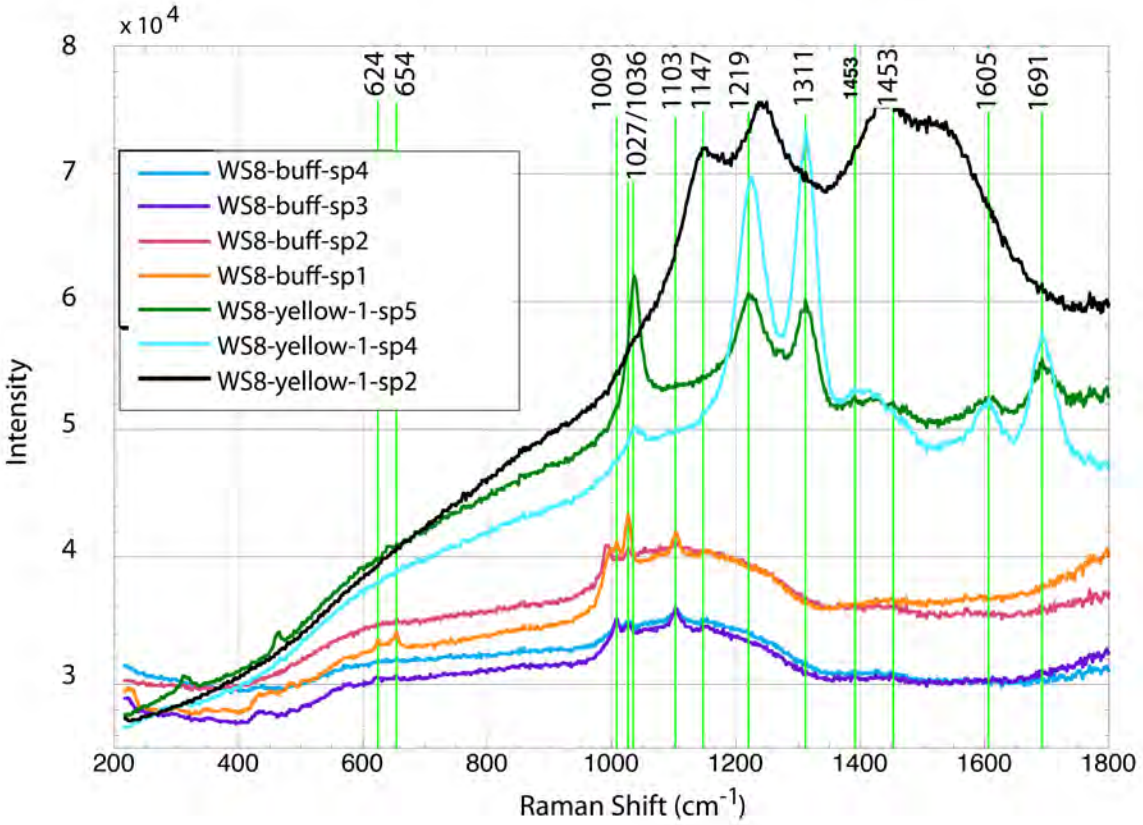
x 10^4
8
7
6
5
4
3
Intensity
624
654
1009
1027/1036
1103
1147
1219
1311
1453
1453
1605
1691
WS8-buff-sp4
WS8-buff-sp3
WS8-buff-sp2
WS8-buff-sp1
WS8-yellow-1-sp5
WS8-yellow-1-sp4
WS8-yellow-1-sp2
200
400
600
800
1000
1200
1400
1600
1800
Raman Shift (cm-1)

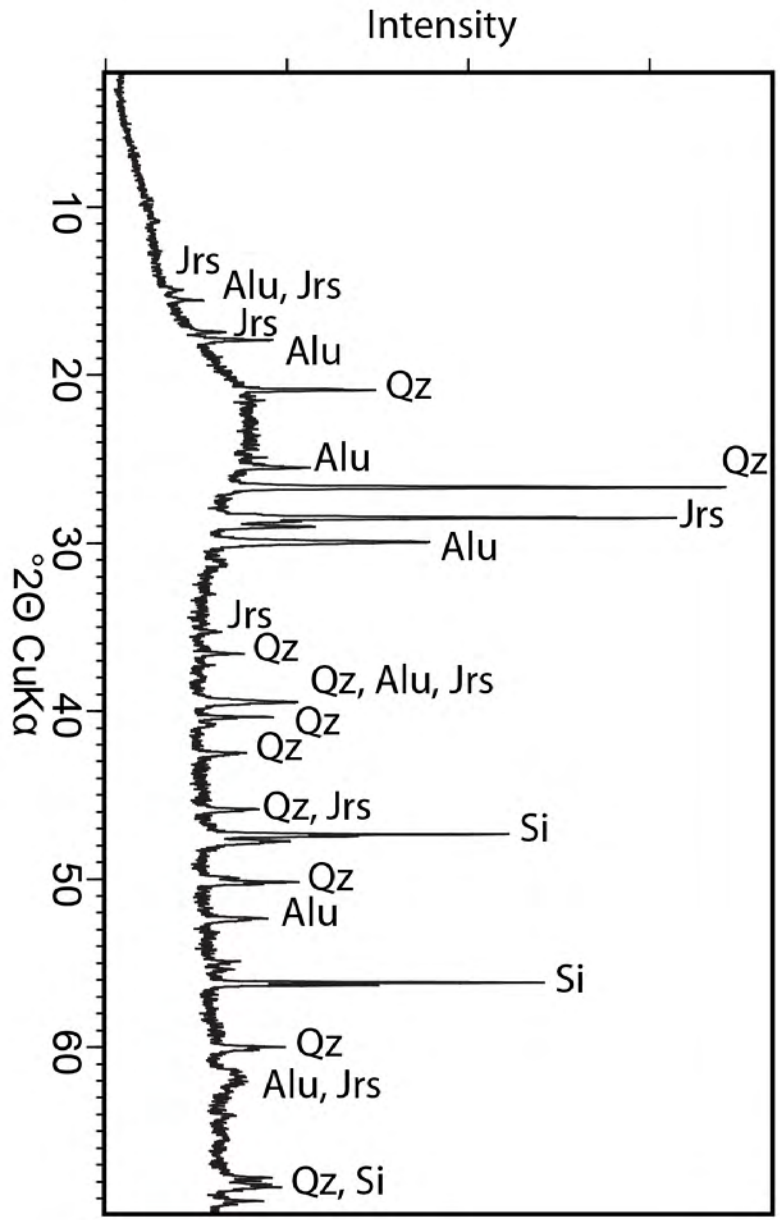
Intensity
°2Θ CuKα
10
20
30
40
50
60
Jrs
Alu, Jrs
Jrs
Alu
Qz
Alu
Qz
Jrs
Alu
Jrs
Qz
Qz, Alu, Jrs
Qz
Qz
Qz, Jrs
Si
Qz
Alu
Si
Qz
Alu, Jrs
Qz, Si

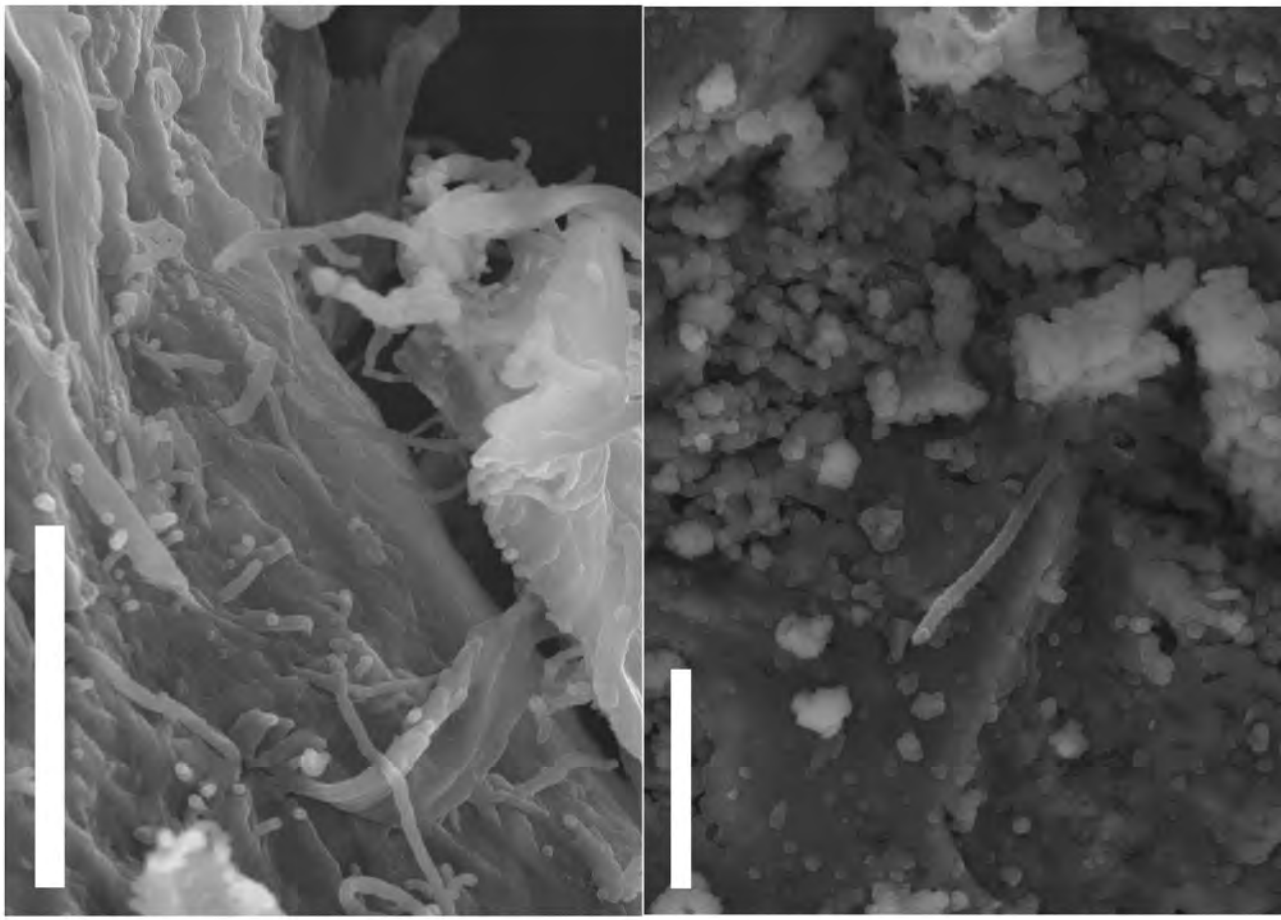

Fig 7

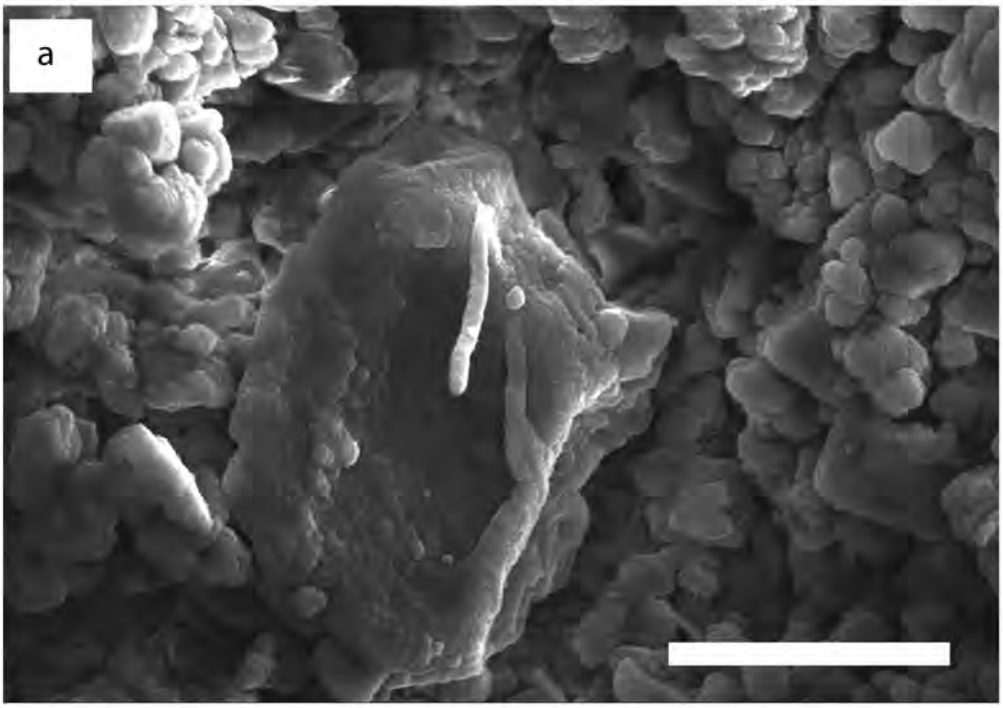

Element	Concentration (wt%)
C	12.09
O	65.88
Na	3.18
Mg	1.54
Al	1.51
Si	2.05
S	10.67
K	0.38
Fe	2.07

!

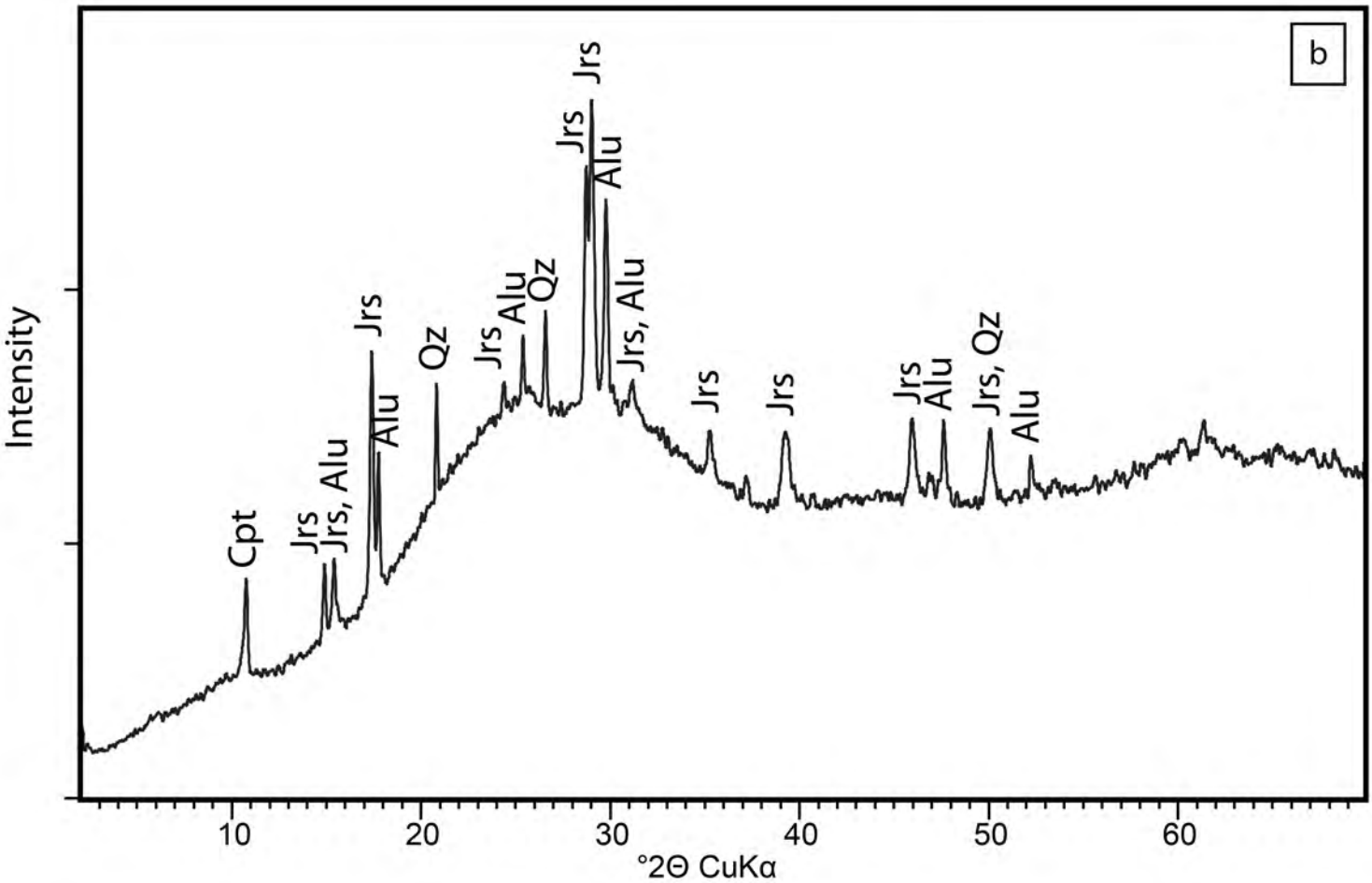

Fig 8

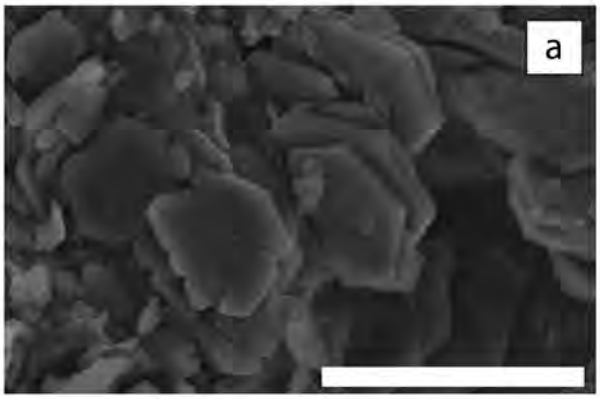

Element	Concentration (wt%)
O	72.06
Na	1.71
Mg	8.79
Al	0.98
Si	1.75
S	14.72

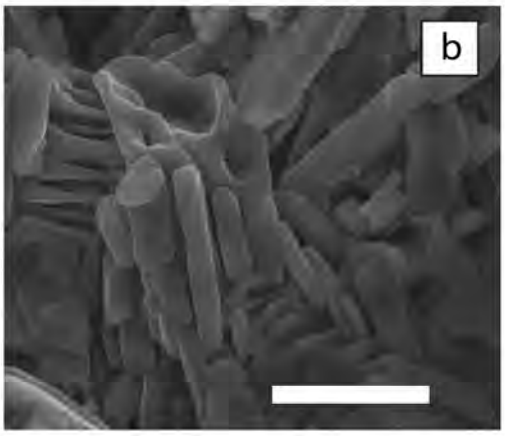

Element	[X] (wt%)
C	12.76
O	71.79
Al	3.15
Si	2.07
S	8.75
K	0.84
Fe	0.64

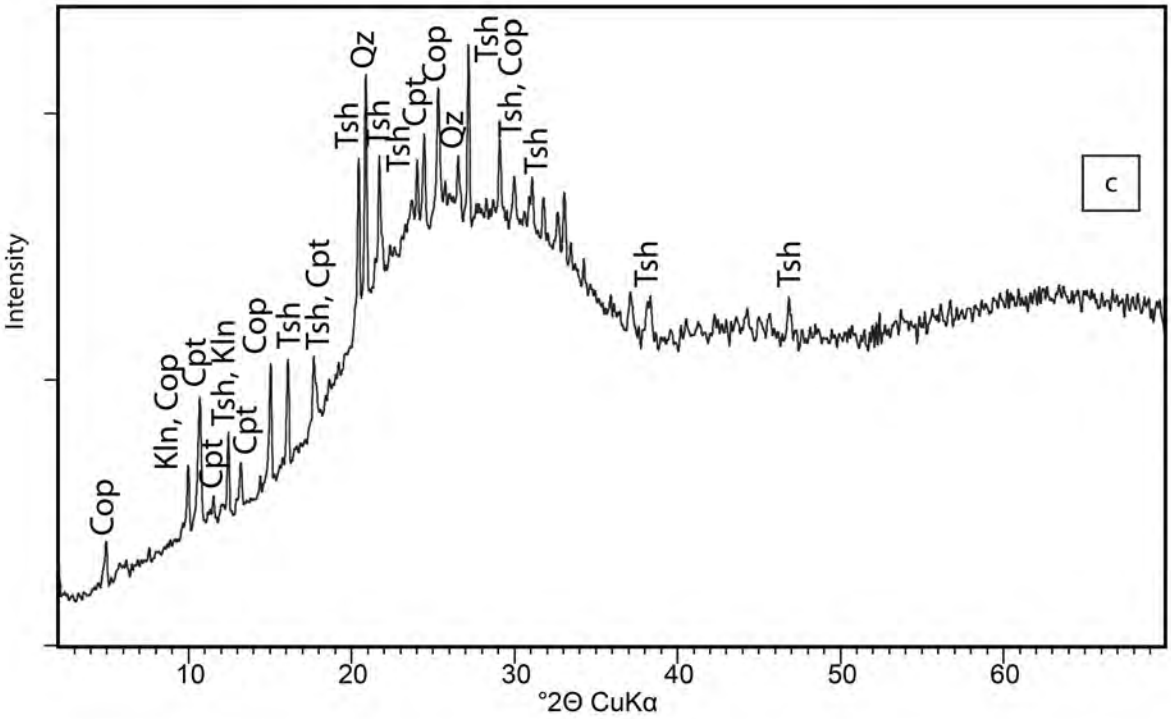

Fig 9

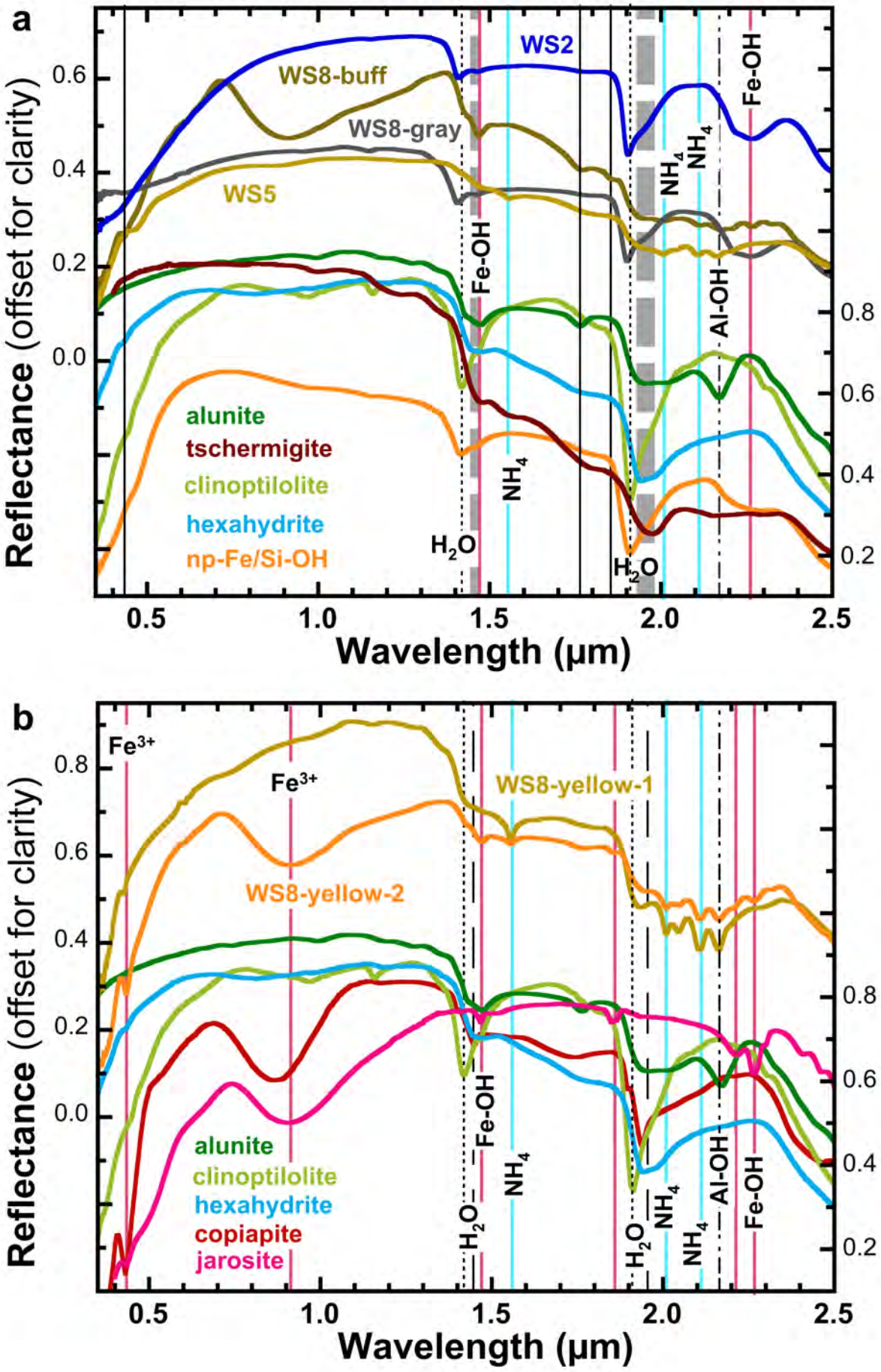
a
WS2
WS8-buff
WS8-gray
WS5
alunite
tschermigite
clinoptilolite
hexahydrite
np-Fe/Si-OH
Fe-OH
NH4
H2O
Al-OH
Reflectance (offset for clarity)
Wavelength (μm)
b
Fe3+
WS8-yellow-1
WS8-yellow-2
alunite
clinoptilolite
hexahydrite
copiapite
jarosite
Reflectance (offset for clarity)
Wavelength (μm)